The impact of B and Zr content on processability, microstructure, and mechanical performance of additively manufactured superalloy IN738LC

MTLA 44 (2025) 102612

Contents lists available at ScienceDirect

Materialia

journal homepage: www.elsevier.com/locate/mtla

Full Length Article

The impact of B and Zr content on processability, microstructure, and mechanical performance of additively manufactured superalloy IN738LC

Abdul Shaafi Shaikh [a,b,*], Bharat Mehta [c], Yiming Yao [a], Eduard Hryha [a]

[a] Chalmers University of Technology, Department of Industrial and Materials Science, Rännvägen 2A, Gothenburg, 41296, Sweden
[b] Electro Optical Systems Finland Oy, Lemminkäisenkatu 36, 20520, Turku, Finland
[c] Thermo-Calc Software AB, Råsundavägen 18, SE-16967, Solna, Sweden

ARTICLE INFO

Keywords:
Superalloy
Additive manufacturing
Cracking
Boron
Zirconium
Creep

ABSTRACT

The minor elements B and Zr have a major impact on the processability and high temperature properties of Ni-base superalloys additively manufactured by the Powder Bed Fusion Laser Beam (PBF-LB) process. To deconvolute the effects of these elements on microcracking and creep life, four variants of the IN738LC superalloy were tested: one with both B and Zr, one with only B, one with only Zr, and one with neither element. PBF-LB microcracking observations were rationalised using a modified Scheil solidification simulation incorporating the solute trapping effects during rapid solidification. Analysis of the microstructures was performed after HIP and heat treatment by SEM-EDX, EBSD, and NanoSIMS. High temperature tensile and creep tests were conducted to ascertain the relative mechanical performance of the four alloys. The alloy variant with both B and Zr resulted in a high crack density of 0.76 mm/mm^2 after PBF-LB processing, whereas variants with only one of the two elements showed significantly reduced crack density of ≈0.02 mm/mm^2. Creep rupture life of the variant with both B and Zr was 66 h at 760°C and 565 MPa, whereas no other variant produced life of more than 38 h, and the variants without either element ruptured in only 6 h. These results indicate that although B and Zr together promote microcracking, they also provide the best creep resistance only when alloyed in combination. The results are discussed in light of the microstructure analysis and with a view towards satisfying the apparently conflicting requirements of creep resistance and crack-free processability.

1. Introduction

Ni-base superalloys such as IN738LC are indispensable in the energy and aerospace industries due to their high temperature strength and endurance. Additive Manufacturing (AM) of these materials presents an opportunity to enhance the function, sustainability, and supply chain robustness of components for high temperature use. However, microcracking during AM processing, especially by the Powder Bed Fusion – Laser Beam (PBF-LB) technique, has held superalloys back from real applications and industrial adoption [1].

A key factor identified in the microcracking susceptibility of several superalloys, especially the legacy polycrystalline alloy IN738LC [2], is the alloying content of minor elements B and Zr. These elements are added to IN738LC as grain boundary strengtheners and are known to be important for the high temperature mechanical performance of the alloy, even though they are added in minute quantities: the B content is in the range of 0.005 to 0.015 wt% and Zr ranges from 0.025 to 0.08 wt %, according to the standard aerospace material specification for cast IN738LC [3]. Cloots et al. identified B and Zr at solidification grain boundaries of as-built IN738LC, leading to the explanation of solidification cracking as the mechanism responsible for microcracking [4]. Gruber et al. and Lindgren et al. investigated microcrack surfaces and found evidence of B and Zr containing oxides, furthering the understanding of the deleterious effects of these elements on microcracking [5,6]. The modification of the composition of IN738LC to exclude grain boundary strengthening elements has also been discussed in light of this understanding [4].

Apart from challenges in microcracking, the creep performance of PBF-LB processed superalloys is generally inferior to that of their conventionally manufactured (cast or wrought) counterparts [7]. Specifically for IN738LC, early tests by Rickenbacher et al. and Kunze et al. showed a deficit in creep strength of PBF-LB IN738LC compared to cast, which was attributed to differences in grain size, texture, as well as γ′ size and morphology [8,9]. These results were corroborated by data from

* Corresponding author.
E-mail address: abdulsh@chalmers.se (A.S. Shaikh).

https://doi.org/10.1016/j.mtla.2025.102612
Received 4 September 2025; Accepted 17 November 2025
Available online 19 November 2025

Wilkes et al. [10]. Analysis by Song et al. concluded that relatively fine grain size in PBF-LB IN738LC compared to cast IN738LC was the main reason for inferior creep resistance of the PBF-LB version, especially in samples built perpendicular to the build direction [11].

Although the PBF-LB processing of IN738LC has been extensively studied with varying levels of B and Zr, the effects of these elements on the microstructure and high temperature strength and creep life have not been well investigated. In the context of modifying minor element content to enhance processability, the performance in creep is essential to measure given that superalloys are high temperature materials. The objective of the current investigation, therefore, is to better understand the influence of B and Zr on microcracking, heat treated microstructure, and high temperature mechanical performance, and especially to deconvolute the individual effects of B and Zr by studying their alloying separately as well as their effect in combination.

2. Materials and methods

Four variants of the IN738LC superalloy were studied in the experiments. The B and Zr content of each alloy was systematically varied to isolate the effect of these minor elements on microcracking and high temperature mechanical properties, as well as for studying the effect of their combined presence or absence from the composition. One alloy was manufactured to contain both B and Zr within the limits of the cast alloy composition as per AMS 5410C [3] and this alloy is designated 738_STD. In the second alloy no B and Zr were added to the composition, resulting in content of these elements below 10 wtppm (the detection limit of the measurement method used) and this alloy is named 738_NBNZ (no B, no Zr). The third alloy included additions of only B in an amount within the AMS5410C limits, whereas Zr was omitted from the composition. This is named 738_NZ (no Zr). The fourth alloy contained no B but included Zr within the limits of AMS5410C and is thus named 738_NB. The alloys were produced in the form of vacuum inert gas melted and gas-atomized powders, with compositions according to Table 1, and particle size distributions between 15 μm and 53 μm. The compositions from virgin powders were measured using Combustion and Fusion methods as per ASTM E1019, and Inductively Coupled Plasma Optical Emission Spectroscopy according to ASTM E2594. Note that minor variations in composition apart from B and Zr are incidental and within the allowed composition range for cast IN738LC. Also note that trace elements Pb, Bi, Se, Te, and Tl were all controlled below the AMS 2280A Class 1 limits due to their deleterious effect on high temperature properties [12,13].

An EOS M290 PBF-LB system was used to manufacture samples for porosity evaluation, microstructure analysis, and mechanical testing. Samples for evaluation of microcracking were manufactured using a custom process parameter set having a laser power of 350W, a scanning speed of 965 mm/s, a hatch spacing of 0.13 mm, and a layer thickness of 40 μm. These parameters result in a relatively high linear energy density E_L of 0.36 J/mm and a volumetric energy density E_v of 70 J/mm^3 intended to provoke overheating and microcracking in the material. Samples for mechanical testing and microstructure analysis were manufactured with the IN738_Core_1.00 process parameters from the machine manufacturer having a 40 μm layer thickness, a hatch spacing of 0.05 mm, a linear energy density of 0.13 J/mm, and a volumetric energy density E_v of 67 J/mm^3. All PBF-LB processing was performed under Ar gas. The sample geometries included cube shaped samples that were used for porosity and microcrack evaluation, as well as 80 mm long and 12 mm diameter blanks for mechanical testing. Since PBF-LB materials often exhibit considerable anisotropy, mechanical testing samples were built in two orientations relative to the building direction (BD). The samples built parallel to the BD are called “vertical” samples and the samples built perpendicular to the BD are called “horizontal” samples. The AM system orientations as well as the sample geometries are shown in Fig. 1.

Following PBF-LB processing, the samples from all alloys were subjected to a combined solution treatment and hot isostatic pressing (HIP) treatment at 1120°C and 200 MPa for 4 h, followed by rapid cooling of around 50°C/min. An ageing heat treatment at 850°C for 24 h was performed in a vacuum furnace, followed by cooling with forced Ar gas at around 20°C/min.

Samples were sectioned and mounted in conductive resin in two orthogonal cross-section orientations: sections parallel to the BD, i.e. XZ or YZ planes, are designated “BD↑” and sections perpendicular to the BD, i.e. XY planes, are designated “BD⊗”. Samples for optical and scanning electron microscopy (SEM) analysis were ground and polished to 1 μm, followed by either electrolytic polishing, electrolytic etching with 10% oxalic acid, or immersion etching with Kalling’s 2 etchant. Samples for Electron Backscattered Diffraction (EBSD) analysis were subjected to further polishing with 0.25 μm fumed silica. An Olympus GX51 optical microscope was used for detecting microcracks in the microstructure samples and for porosity analysis. SEM analysis was performed on a Zeiss GeminiSEM 450, with an Oxford Symmetry detector for Electron Backscattered Diffraction (EBSD) analysis. A step size of 0.5 μm was used for EBSD mapping, and data analysis was performed with Oxford AztecCrystal using a criterion of 10° misorientation for grain determination. Energy Dispersive X-ray Spectroscopy (EDX) in SEM was performed with the high solid-angle Bruker XFlash FlatQUAD detector, inserted laterally between the sample and SEM pole piece. A conventional Bruker XFlash7 detector was also used for EDX analysis in SEM.

A Cameca NanoSIMS 50L mass spectrometer was utilised for secondary ion mass spectrometry (NanoSIMS) analysis. Cs^+ ions were used as the primary ions. Samples for NanoSIMS analysis were prepared similar to metallographic samples for SEM analysis (polished and etched). As is typical for NanoSIMS, the microstructural regions of interest were implanted with Cs^+ ions prior to analysis to increase secondary ion yield.

Cylindrical machined specimens with gauge diameter of 6 mm, parallel length of 30 mm, and gauge length of 24 mm were used for stress rupture and creep rupture testing as per ASTM E139. Elevated temperature tensile testing according to ISO 6892-2 was performed using machined cylindrical samples with 5 mm gauge diameter and 25 mm gauge length. Tensile tests were conducted using crosshead control with an equivalent strain rate of 0.00025 s^{-1} until yield, switching to

Table 1
Chemical composition of the powder alloys in wt.%. The typical composition range for cast IN738 according to AMS5410C is also shown.

		Ni	Cr	Co	Al	Ti	Mo	W	Ta	Nb	Si	S	Zr	B	C
IN738 AMS5410C	min, wt.%	Bal	15.7	8.0	3.20	3.20	1.50	2.40	1.50	0.60	-	-	0.025	0.005	0.09
	max, wt.%	Bal	16.3	9.0	3.70	3.70	2.00	2.80	2.00	1.10	0.30	0.015	0.080	0.015	0.20
738_STD	at.%	Bal	17.4	8.5	6.82	4.34	1.09	0.85	0.50	0.64	0.08	0.004	0.017	0.068	0.49
	wt.%	Bal	15.9	8.9	3.24	3.65	1.85	2.76	1.61	1.04	0.037	0.002	0.027	0.013	0.10
738_NBNZ	at.%	Bal	17.8	7.9	6.98	3.97	1.01	0.76	0.51	0.43	0.05	0.005	-	-	0.47
	wt.%	Bal	16.3	8.2	3.32	3.35	1.71	2.47	1.63	0.70	0.024	0.003	<0.001	<0.001	0.10
738_NZ	at.%	Bal	17.1	8.0	6.76	3.90	0.99	0.74	0.51	0.54	0.07	0.004	-	0.050	0.51
	wt.%	Bal	15.7	8.3	3.21	3.29	1.67	2.41	1.62	0.88	0.033	0.002	<0.001	0.010	0.11
738_NB	at.%	Bal	17.3	7.9	6.74	4.05	0.95	0.75	0.50	0.50	0.06	0.004	0.040	-	0.57
	wt.%	Bal	15.9	8.3	3.20	3.41	1.61	2.47	1.58	0.81	0.031	0.002	0.065	<0.001	0.12

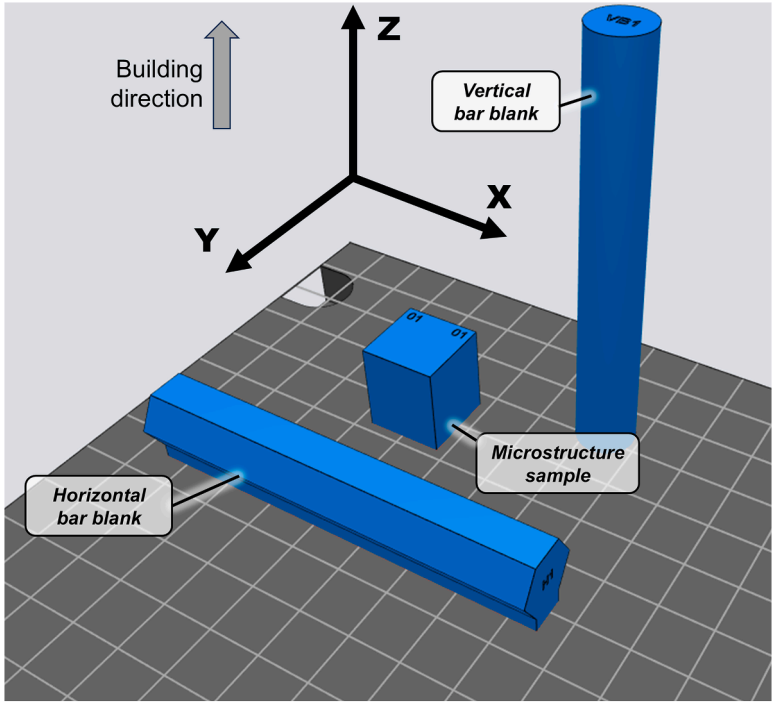

Fig. 1. Orientations and geometries of test specimens manufactured for experiments. Grid is 1 cm.

0.0014 s^{-1} until fracture. Two samples were tested per alloy per orientation per test temperature.

Thermo-Calc 2025a and the TCNI12 database were used to simulate the solidification behaviour of the various alloys. Scheil solidification calculations were performed using a step of 1 K with the phases LIQUID, FCC_L12 (γ phase), FCC_L12#2 (γ′ phase), and FCC_L12#3 (MX carbonitride phase) selected according to the reported as-solidified microstructure of IN738LC in PBF-LB [6,14]. More details on the modelling inputs are given in Sections 3.1 and 4.2.

3. Results

3.1. Processability and microcracking

Evaluation of microcracking susceptibility for the four IN738LC variants was made based on plain polished micrographs, which can be seen in Fig. 2. A clear difference between the four variants was observed, where 738_STD shows a high frequency of microcracks, whereas no microcracks could be found in the 738_NBNZ cross-section. The 738_NZ and 738_NB alloys present a much lower incidence of microcracking compared to 738_STD. Low magnification overview micrographs of each sample are given in Appendix Fig. A1 to demonstrate the widespread nature of microcracking or lack thereof. Quantification of the defect % and crack density was performed by image analysis, the results of which are shown in Table 2. Defect percentage is the ratio of area of black pixels to white pixels x 100 (after binarizing the image) and crack density is the ratio of the sum of crack length to the area over which analysis was carried out. The highest crack density (and consequently highest defect %) was observed for 738_STD, and this alloy also showed the largest maximum defect size. The crack density and defect % of the 738_NZ and 738_NB alloys were significantly lower, however microcracks of around ≈ 100 μm in size could still be found. No cracks were found in the cross-section of the 738_NBNZ alloy, and only round pores of maximum 25 μm diameter were seen, resulting in a very low 0.004% of defects. The results point to a clear trend that 738_STD (bearing both B and Zr) showed the highest microcracking susceptibility. The alloys 738_NZ and 738_NB (containing only one of either B or Zr) showed substantially reduced microcracking susceptibility relative to 738_STD, whereas 738_NBNZ did not show susceptibility to microcracking under the current experimental conditions.

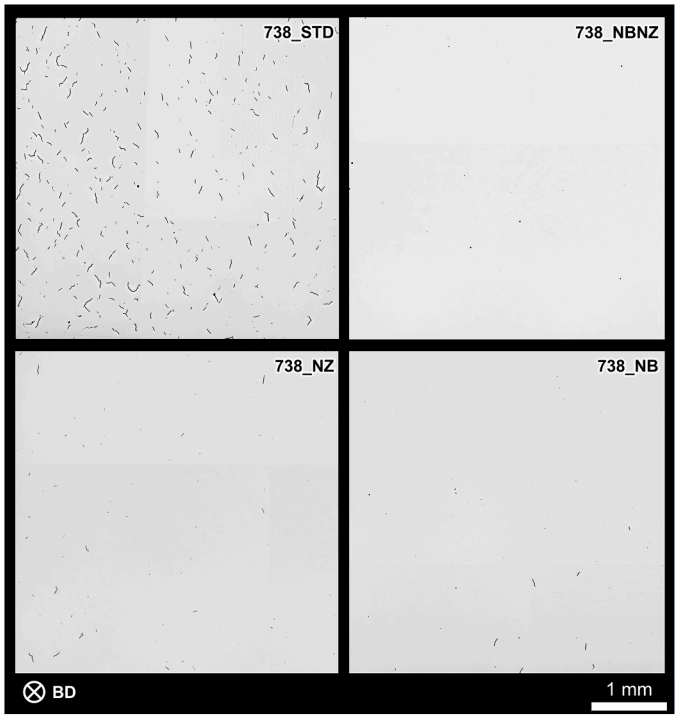

Fig. 2. Optical micrographs of plain polished XY cross-sections of all 4 alloy variants in as-built condition, showing the difference in microcracking between variants.

Solidification simulations of the alloy variants by Scheil calculations was performed using Thermo-Calc to gain insights into the observed microcracking behaviour, and to determine Sindo Kou's Solidification

Table 2
Porosity and crack density measurements from the XY cross-sections of the 4 alloys.

Alloy	Section	Defect %	Crack density (mm/mm^2)	Max. Defect size (μm)
738_STD	XY	0.283	0.76	217
738_NBNZ	XY	0.004	-	25
738_NZ	XY	0.007	0.02	115
738_NB	XY	0.010	0.02	84

Cracking Index (SCI) for each alloy [15]. The SCI is often used in welding, casting, and additive manufacturing of alloy systems to determine an alloy's susceptibility to hot tearing or solidification cracking. The SCI is calculated from Scheil solidification curves and is given by $\left|\frac{dT}{df_s^{1/2}}\right|$ where T is the temperature and f_s is the corresponding fraction of solid. This value is typically determined for the last part of solidification, where f_s approaches 1. Note that the classic Scheil-Gulliver solidification calculation is based on the assumptions of perfect mixing in the liquid, no diffusion in the solid, and equilibrium at the liquid-solid interface [16]. These assumptions are not valid under rapid solidification conditions such as those of PBF-LB. When solidification velocity is fast, there is not enough time for solute elements to diffuse into the liquid phase and homogenize, which renders the assumption of perfect mixing in the liquid untrue. The solute is therefore trapped at the interface, which also means that the liquid-solid interface is no longer at equilibrium. Hence, the Scheil calculations used in the results presented herein utilize a modified Scheil simulation based on the Aziz model [17,18] which accounts for the "solute trapping" effect, and is expected to provide a more realistic model of solidification in PBF-LB. This model requires the speed of the heat source (laser scanning speed = 965 mm/s) and the angle between the scanning direction and solidification direction (α = 45°) as user inputs. Thermo-Calc was also used to calculate the equilibrium solidus and liquidus temperatures for the four variants, in addition to the solidus and liquidus temperatures from the non-equilibrium Scheil simulation. These results are summarized in Fig. 3 and Table 3.

The Scheil simulations with solute trapping show that the 738_STD alloy has the widest solidification range under the simulated rapid solidification conditions – see Table 3. The T vs f_s curves in Fig. 3 (a) also show that relative to the other alloys, 738_STD retains a small liquid fraction down to lower temperatures, which results in a steeper gradient of the Scheil curve at the end of solidification ($f_s^{\frac{1}{2}}$ value from 0.90 to 0.99) resulting in the highest value of SCI. According to Kou, the physical interpretation of this solidification behaviour is that the remaining liquid at the solidification grain boundaries for 738_STD presents too narrow a channel for further liquid feeding, resulting in crack formation when the strain from cooling contractions acts on the liquid film. The 738_NZ and 738_NB alloys have smaller solidification ranges (both equilibrium and from Scheil) and slightly flatter slopes in the T vs $f_s^{\frac{1}{2}}$ curves, and therefore lower values of SCI. The 738_NBNZ was found to have the smallest value of SCI, and the lowest Scheil and equilibrium solidification temperature ranges. The trend of SCI and Δ_S values agrees well with the observed microcracking behaviour.

3.2. As-built microstructure

Examination of the as-built condition of all four alloys by SEM revealed fine cellular-dendritic microstructures, as shown in Fig. 4. As is typical for PBF-LB Ni-base alloys, grains were elongated in the BD due to epitaxial growth across layers, and dendrites were often aligned with the growth direction. No secondary dendrite arms were observed. Bright contrast at interdendritic regions was observed in back-scattered electron (BSE) imaging which indicates the presence of primary carbides, see Fig. 4. No systematic differences in the solidification microstructure from as-built samples could be determined at SEM resolution, and no evidence of γ′ precipitation was found. High resolution characterization of the as-built microstructure of IN738LC corresponding to (738_STD) can be found elsewhere [5,6,14,19].

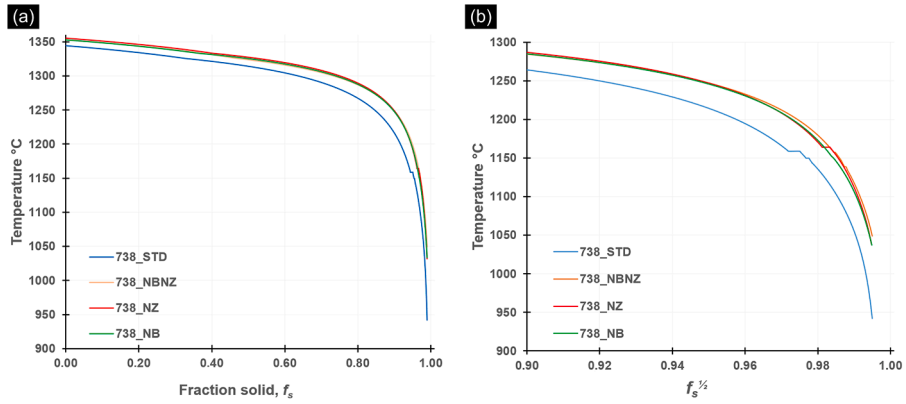

Fig. 3. (a) Temperature vs fraction solid f_s for the 4 alloys from Scheil solidification simulations with solute trapping using Thermo-Calc 2025a; (b) Temperature vs $f_s^{½}$ curves ($f_s^{½}$ = 0.9-1.0) for the 4 alloys used for calculating the Kou Solidification Cracking Index.

Table 3
Liquidus temperatures T_L, solidus temperatures T_S, solidification ranges Δ_S, for equilibrium (EQ) and Scheil simulations from Thermo-Calc 2025a, as well as Solidification Cracking Index (SCI) for the four alloys.

	$T_{L,\ EQ}$,°C	$T_{S,\ EQ}$,°C	$\Delta_{S,\ EQ}$,°C	$T_{L,\ Scheil}$,°C	$T_{S,\ Scheil}$,°C	$\Delta_{S,\ Scheil}$,°C	SCI $_{0.9<fs<0.99}$
738_STD	1347	1217	130	1345	942	403	14096
738_NBNZ	1354	1301	53	1353	1049	304	7983
738_NZ	1357	1243	114	1355	1032	323	9338
738_NB	1354	1269	85	1353	1034	319	8157

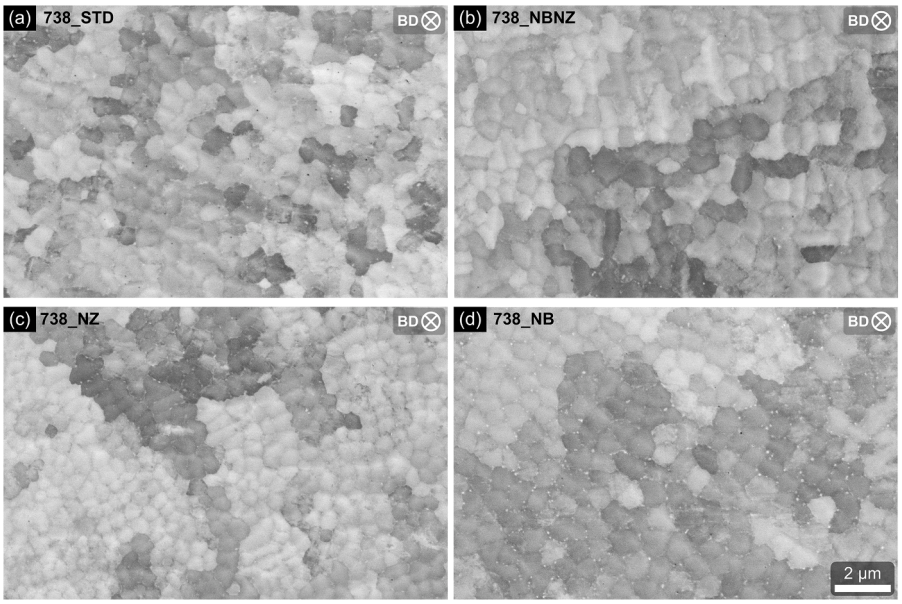

Fig. 4. SEM BSE micrographs showing the as-built microstructure of (a) 738_STD; (b) 738_NBNZ; (c) 738_NZ; (d) 738_NB in the plane perpendicular to the building direction.

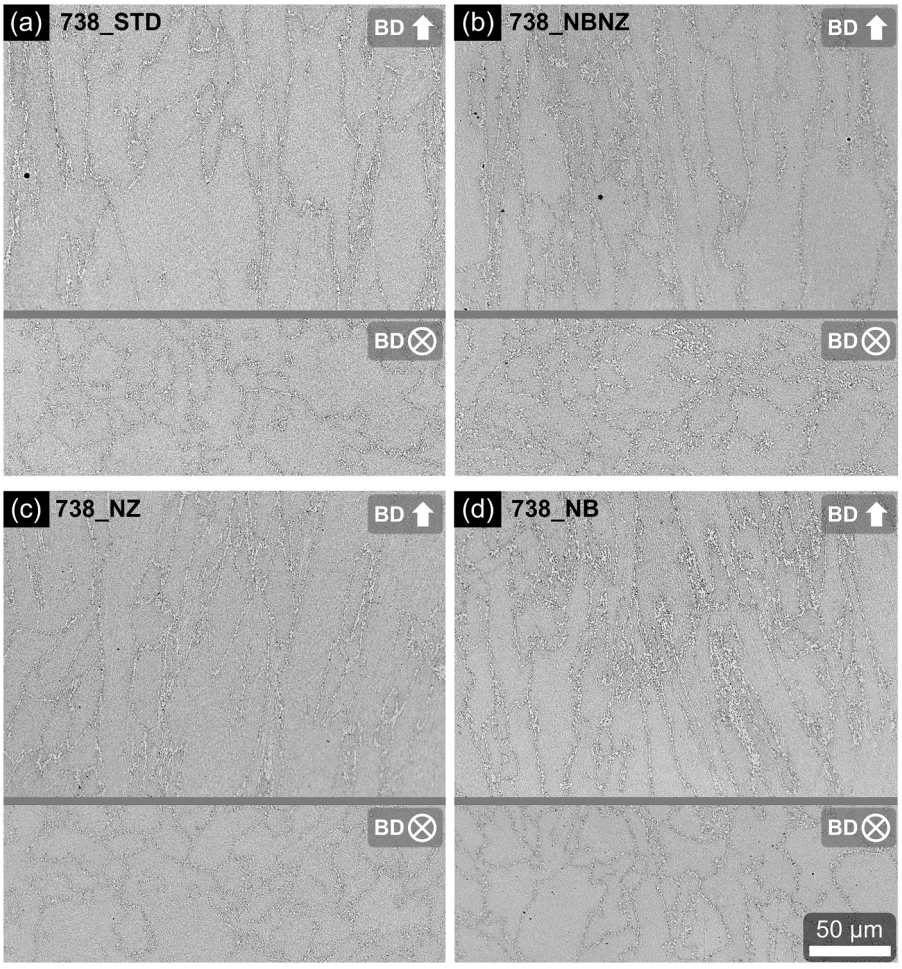

Fig. 5. Optical micrographs showing the grain structure in planes perpendicular and parallel to the building direction after HIP and ageing heat treatment for (a) 738_STD; (b) 738_NBNZ; (c) 738_NZ; (d) 738_NB. Electrolytic etch with oxalic acid.

3.3. Heat treated microstructures

The heat treatment applied to samples of all alloy variants included a HIP at 1120°C and 200 MPa for 4 h, intended to densify the material and heal the cracks, so that mechanical performance of the IN738LC variants could be compared without the influence of microcracks. Plain polished overview micrographs of densified microstructure sample cross-sections are shown in Appendix Fig. A4. The heat treatment temperature of 1120°C is taken directly from the standard solution heat treatment used for the casting material though it is below the γ' solvus temperature of IN738LC. Similarly, the ageing temperature of 850°C is according to the typical heat treatment regime stipulated for the casting alloy [2,3].

Optical micrographs of XY and ZY cross-sections of all four alloy variants (see Fig. 5) show elongated grains in the BD, and apparent fine irregular grain morphology perpendicular to the BD, as is commonly observed for PBF-LB Ni-base alloys. Light contrast at the grain boundaries indicates the presence of grain boundary phases. No signs of grain growth were observed and the grain structure is similar to the as-built grain structure owing to the sub-solvus "solution" treatment temperature, which precludes any grain growth. No systematic differences in the microstructures were apparent in the analysis by optical microscopy.

The focus in microstructure characterization was on the possible differences in microstructure between the four alloys, and the following results focus on XY cross-sections which are more feature-rich due to the higher density of grain boundaries where differences in B and Zr content would be expected to cause changes in the microstructure.

Table 4
Equivalent circle diameter grain size distribution of the 4 different alloys after heat treatment, from EBSD measurements. A misorientation of 10° was used for grain determination and CSL boundaries were not included.

Alloy	Section	Grain size *, μm				Twinned grains fraction (%)
		Quartile 1	Median	Mean	Quartile 3	
738_STD	XY	3.5	6.3	11.1	12.9	1.4
738_NBNZ	XY	3.6	6.3	10.8	12.8	36.1
738_NZ	XY	3.5	6.2	11.0	12.8	1.7
738_NB	XY	3.6	6.4	11.0	13.2	20.6

* Equivalent circle diameter grain size

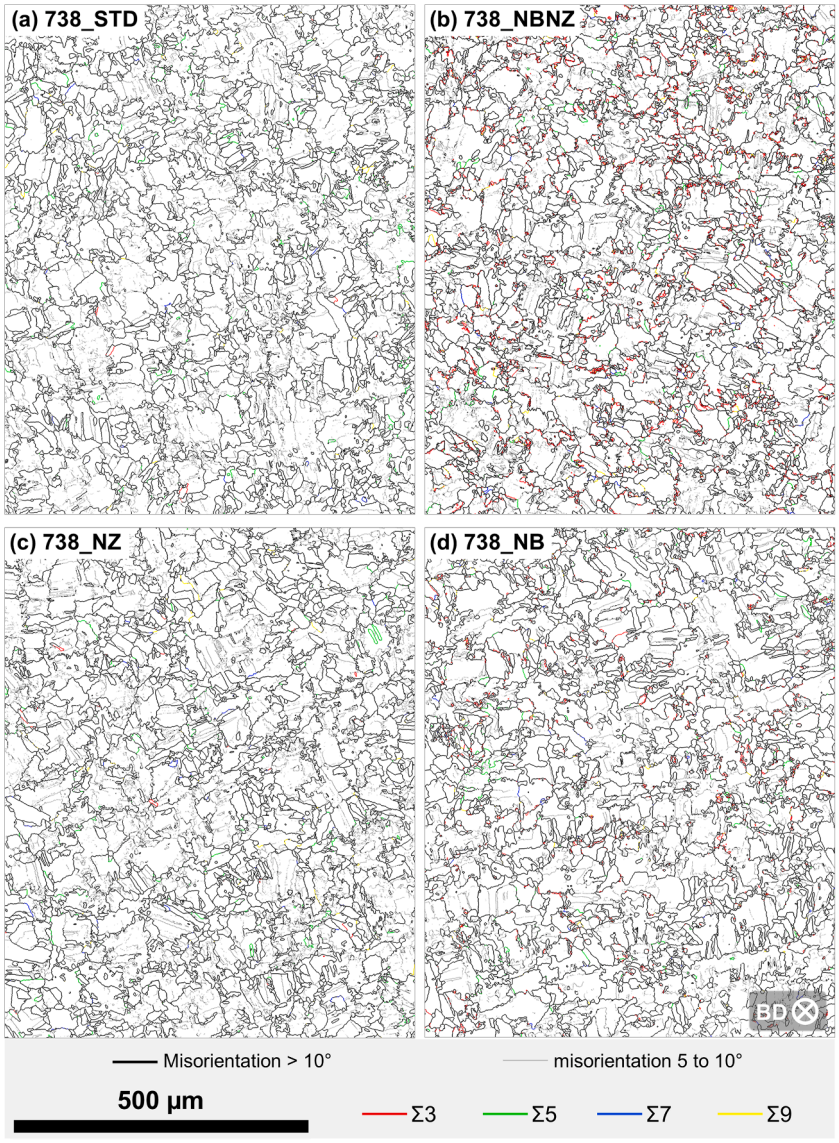

Fig. 6. EBSD maps showing grain structure perpendicular to the building direction for the 4 alloy variants after heat treatment (a) 738_STD; (b) 738_NBNZ; (c) 738_NZ; (d) 738_NB.

Detailed analysis of the grain structures of the alloy variants after heat treatment was performed using EBSD mapping. Grain boundary maps showing the grain structures can be seen in Fig. 6. The grain size was fine and the morphology of the grains was irregular. A high incidence of subgrain boundaries or low-angle grain boundaries with misorientation below 10° can be seen, likely due to the sub-solvus heat treatment, which did not fully homogenize the as-solidified microstructure nor induce any grain growth. The grain size distribution of all four alloys was analysed from the EBSD measurements, and mean equivalent circle diameter grain size of around 11 μm was found for all alloys. Note that parent grain size (excluding any twin boundaries) is represented. More detailed analysis of the grain size distribution is given in Table 4, showing a high degree of similarity between the four alloys.

Samples from all four alloys showed a strong [100] texture as shown by the pole figures in Appendix Fig. A2. Such texture is very commonly observed in PBF-LB Ni-base alloys [7]. A distinction between the alloys was observed in terms of coincidence site lattice (CSL) boundaries, which can be seen from the coloured boundaries in Fig. 6. The samples of 738_NBNZ and 738_NB displayed a high number of small CSL boundaries relative to the samples of 738_STD and 738_NZ. This can also be seen from the twinned grain boundary fraction in Table 4. The highest fraction of grains featuring twins was found in 738_NBNZ while 738_STD and 738_NZ showed only 1.4% and 1.7% of grains having twins, respectively. The relative frequency of CSL boundaries displayed in Fig. 7 further shows that the highest frequency was for Σ3 (twin) boundaries, and this was observed in the 738_NBNZ sample. Fig. 7 also shows that the frequency of low angle boundaries (5° to 10° misorientation) was higher in 738_STD and 738_NZ and lower in 738_NBNZ and 738_NB.

A closer view of the 738_NBNZ grain boundary EBSD map is shown in Fig. 8 (a). The map shows that the observed Σ3 boundaries were short sections appearing as bulges out of the high angle grain boundary. Yellow arrows point to two examples of regions where a proliferation of bulging boundaries can be seen, suggesting that grain boundary migration had begun to take place. A high magnification SEM BSE image of 738_NBNZ in Fig. 8 (b) also shows small twins in the microstructure, confirming the observation from EBSD.

Fig. 9 shows SEM micrographs of all four alloy variants using the InLens secondary electron detector, displaying the typical microstructural features observed in each alloy within grains and at grain boundaries. All the alloys featured intragranular γ′ with irregular spherical morphology and size of around 0.5 μm. Smaller γ′ precipitates of 0.1 to 0.2 μm in size were also observed. The 738_STD and 738_NZ alloys both exhibited a lamellar phase at the grain boundary, which was not observed for the 738_NBNZ and 738_NB alloys. As the varying B and Zr contents are expected to have their main effect at grain boundaries, the microstructure characterization effort was concentrated on the analysis of grain boundary features.

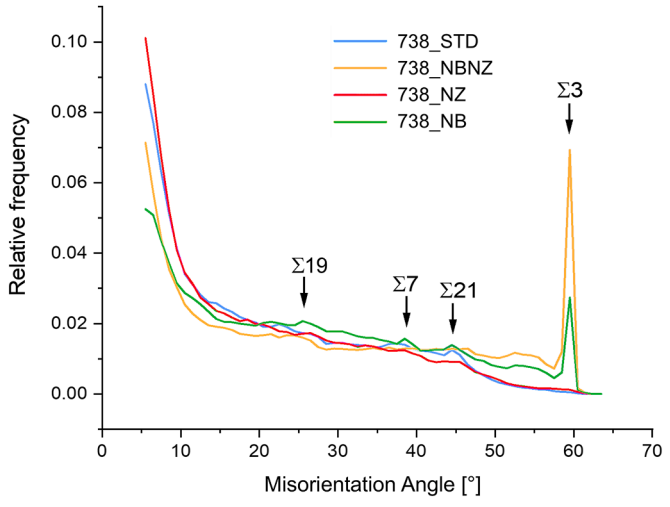

Fig. 7. Relative frequency of misorientation of neighbour grain boundary pairs for the 4 alloys in microstructures after heat treatment, from EBSD measurements.

An SEM micrograph and corresponding EDX map of the 738_STD microstructure is shown in Fig. 10. The sample was prepared with Kalling's 2 etchant to etch away the γ and γ′ phases and reveal the grain boundary structure and non-metallic phases. Many small intragranular carbide particles can be observed in the microstructure from the C and Ta EDX maps. These are Ta, Ti, and Nb-rich MC carbides typically formed at interdendritic regions during solidification, which remain in the microstructure through the heat treatment due to their high thermodynamic stability [20]. MC carbides are also observed at the grain boundaries, which are slightly larger in size due to coarsening during heat treatment. The lamellar phase seen at the grain boundary was observed to be rich in Cr and B, with some content of C as well. Cr-rich phases in IN738LC are most often reported to be either $M_{23}C_6$ carbides or various borides [21]. Grain boundary γ′ can also be observed from the Ni and Al maps.

Note that all grain boundary phases were observed to be very small in size, typically less than 1 μm, which necessitated the use of the high solid angle EDX detector, and a low accelerating voltage of 3 kV to enhance the lateral resolution enough to observe the fine microstructure. Additionally, to confirm the distribution of C, B, and Zr in the microstructure, the 738_STD metallographic sample was also analysed by NanoSIMS, as shown in Fig. 11.

As topographic imaging at high magnification is not possible in the NanoSIMS instrument, the grain boundary structures of the regions of interest are shown by schematic diagrams in Fig. 11. Ions of C^- and BO^- were detected in the NanoSIMS analysis, indicating higher concentration of C and B at grain boundaries relative to grain interiors, along with high intensity of C and B signals at certain regions presumed to be grain boundary phases. In the Site 1 of Fig. 11 (a) the bottom right region shows an elongated grain boundary region with C and B concentration, possibly similar to the lamellar phase observed in SEM-EDX in Fig. 10. Secondary ions of ZrO^- were also detected, suggesting Zr-rich particles at the grain boundary, but no corresponding C or B was detected at those locations. One Zr-rich particle was also spotted away from the grain boundary, seen in the upper half of the composite map of Site 1. This may indicate the presence of Zr-containing phases such as oxides or sulphides, however these could not be confirmed experimentally.

A further NanoSIMS map labelled Site 2 is shown in Fig. 11 (b). Similar to Site 1, C and B were observed clearly at grain boundaries. Zr concentration was also found at the grain boundaries, however in this case, the Zr was clearly co-located with C and B. This is shown in the composite maps and at line scans A and B, where counts of each of the C, B, and Zr containing secondary ions can be seen increasing simultaneously. This observation suggests the presence of phases containing at least all three grain boundary elements, e.g. carbides or borides, or several phases located close together, as has been observed by Theska et al. in other Ni-base superalloys [22].

The microstructure of the 738_NBNZ is shown in Fig. 12. Similar inter-granular and intra-granular MC carbides were observed as in 738_STD, and Cr, Mo, and W-rich grain boundary carbides were also observed which are likely $M_{23}C_6$ carbides. As expected, no B or Zr-rich phases were identified in the microstructure.

Fig. 13 (a) shows the microstructure of the 738_NZ alloy using SEM BSE imaging, on a sample where the γ phase was etched by electrolytic etching using Oxalic acid. The light grey contrast shows the γ′ phase, and a dark grey contrast shows several lamellar phases at the grain boundary. MC carbides can also be seen in white contrast. In addition to the lamellar phase, very small 200 nm sized Cr and B-rich particles were also observed, as shown in Fig. 13 (b).

The analysis of the 738_NB microstructure showed the presence of Ta, Nb, Ti-rich MC carbides at grain boundaries, as well as Cr-rich carbides. The microstructure and corresponding EDX map are shown in

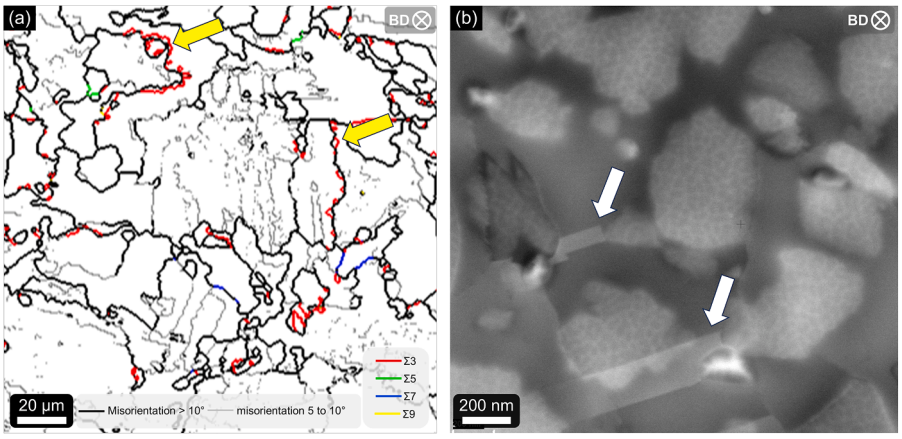

Fig. 8. (a) EBSD map of 738_NBNZ after heat treatment, with yellow arrows pointing to Σ3 CSL boundaries bulging out from high angle grain boundaries; (b) SEM BSE micrograph of electropolished 738_NBNZ after heat treatment, with white arrows showing small twins observed in the microstructure.

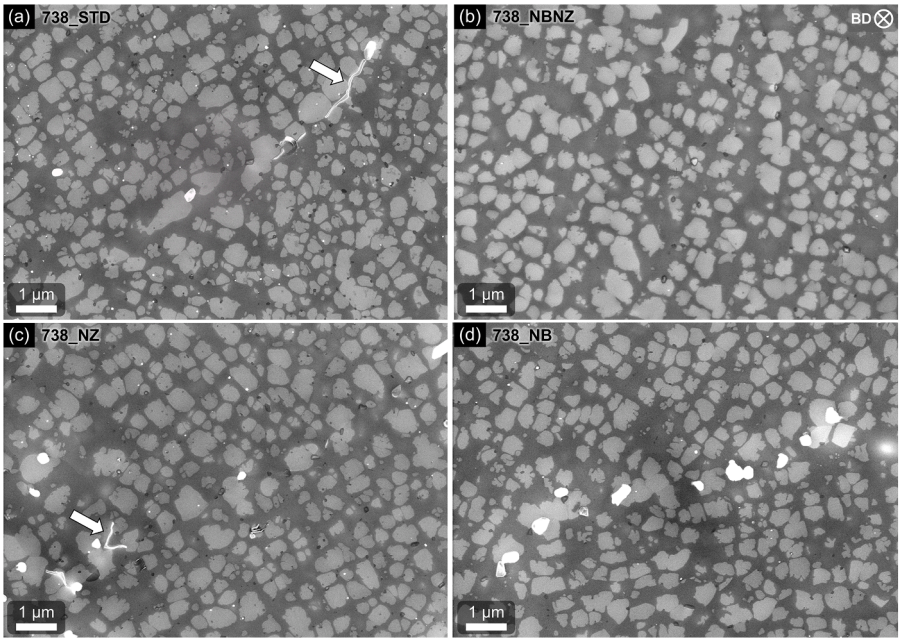

Fig. 9. SEM micrographs showing the microstructure of (a) 738_STD; (b) 738_NBNZ; (c) 738_NZ; (d) 738_NB. Micrographs taken using InLens detector on electropolished specimens sectioned perpendicular to the build direction. Arrows point to a lamellar phase observed at grain boundaries in 738_STD and 738_NZ.

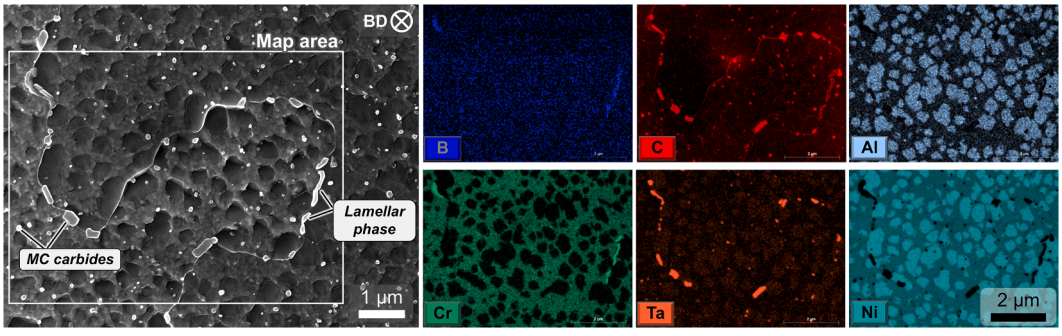

Fig. 10. SEM InLens micrograph and corresponding EDX maps showing the microstructure of the 738_STD alloy after heat treatment. Sample etched with Kalling's 2 etchant to reveal grain boundary phases.

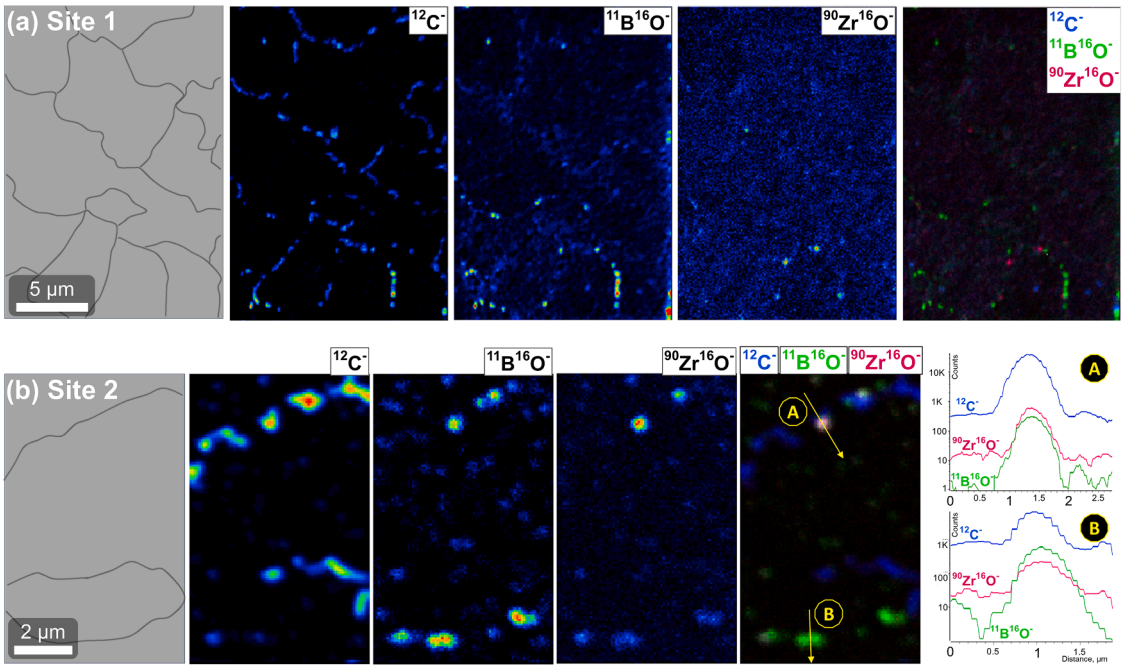

Fig. 11. NanoSIMS maps showing distribution of secondary ions in the heat treated 738_STD microstructure at two sites. Schematic diagrams on the left show the position of grain boundaries for reference. Composite maps on the right show the overlaid distribution of detected secondary ions.

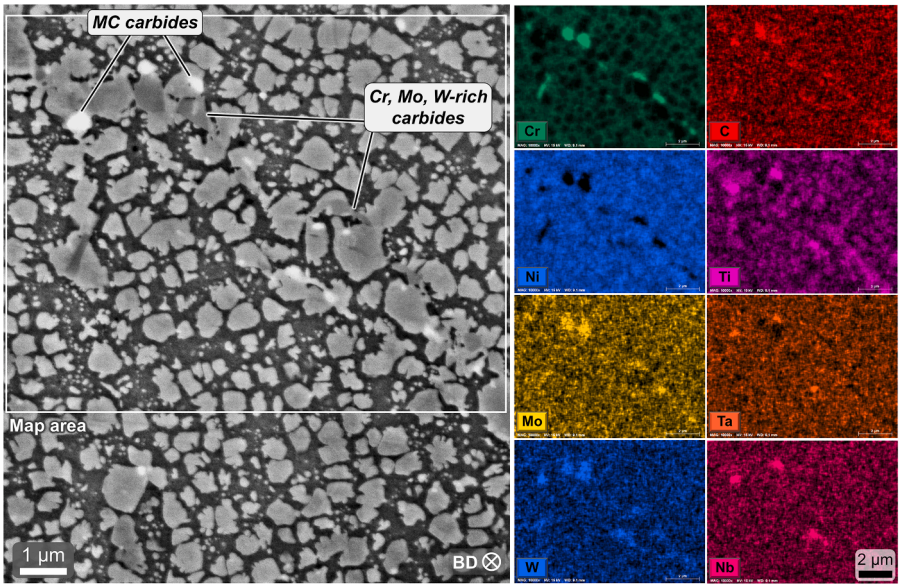

Fig. 12. SEM BSE micrograph and corresponding EDX maps showing the microstructure of the 738_NBNZ alloy after heat treatment. Sample electroytically etched with Oxalic acid.

Fig. 14. Zr was mapped with higher accelerating voltage of 5 kV to be able to detect the Zr-Lα line. While detection of the Zr is challenging due to the small amount of the element in the alloy (only 0.040 at%) the EDX maps indicate enrichment of Zr in some of the carbide phases (marked in the SEM image by yellow arrows) including at the grain boundary. Some spots of Zr enrichment were also found from within grains, where no obvious phases could be observed (shown by black arrows in Fig. 14). This is possibly explained by the characteristic X-ray signal detected by EDX coming from deeper below the surface of the sample compared to back-scattered electrons, or by the presence of fine Zr-oxide particles at prior interdendritic regions [5]. The analysis suggests Zr partitioning to particulate phases both at the grain boundary and within grains.

3.3. Mechanical performance

Creep resistance across a range of elevated temperatures is a critical property for superalloys such as IN738LC, therefore creep rupture tests were carried out at two dissimilar test conditions to determine the difference in creep resistance between the four alloy variants. A low temperature - high stress condition of 760°C with 565 MPa applied stress was tested, as well as a high temperature - low stress condition of 982°C and 151 MPa applied stress. For each condition, both horizontal and vertical bars were tested, since AM superalloys are known to have anisotropic creep performance [8,23]. Each test was performed in duplicate (and where possible in triplicate) to reduce the likelihood of experimental errors.

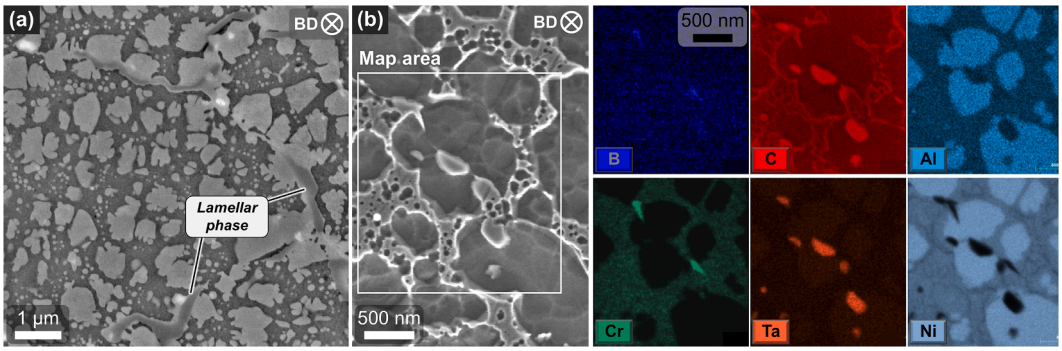

Fig. 13. (a) SEM BSE micrograph showing microstructure of the heat treated 738_NZ alloy; (b) SEM SE micrograph and corresponding EDX maps showing distribution of alloying elements in the microstructure. Sample in (a) was electrolytically etched with Oxalic acid, specimen in (b) was immersion etched with Kalling's 2 etchant.

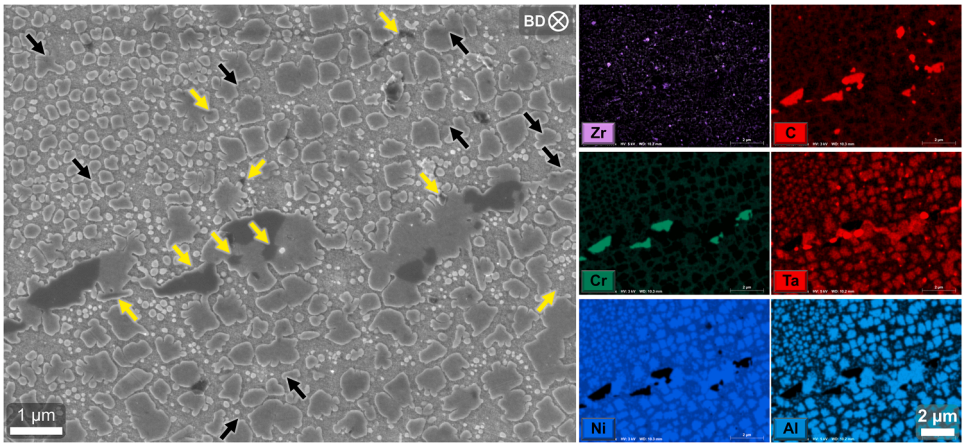

Fig. 14. SEM InLens micrograph and corresponding full frame EDX maps showing the microstructure of the 738_NB alloy after heat treatment. Sample etched electrolytically with Oxalic acid. Yellow and black arrows point to regions of high Zr concentration. Maps of C, Cr, and Ni acquired with 3 kV and maps of Zr, Al, and Ta with 5 kV accelerating voltage.

The creep rupture test results are shown in Fig. 15, and it is evident that the highest time to rupture in all conditions and orientations was achieved by the 738_STD alloy, containing both B and Zr, despite higher microcracking in the as-built condition for that alloy. The 738_NZ alloy showed the second highest rupture life but failed at times consistently lower than the 738_STD alloy. The 738_NB alloy exhibited very poor rupture life by comparison, and the 738_NBNZ alloy was found to have the worst performance of all the tested alloys, with some horizontal samples failing less than 30 minutes after loading. The trend of creep rupture life among alloy variants was valid for both orientations – horizontal and vertical – and both test conditions, however horizontal rupture lives were in general very low relative to vertical. Overall, the creep rupture results showed low variance between duplicate samples, as indicated by the error bars in Fig. 15.

Detailed results from the creep testing are given in Appendix Table A1. It was notable that apart from higher rupture life, the B bearing alloys (738_STD and 738_NB) also showed higher values of rupture elongation and area reduction, especially at the 760°C / 565 MPa test condition.

Results from additional creep tests that were run as creep strain tests are shown in Fig. 16. Only vertical orientations were tested as the horizontal orientations show very short creep lives, and the 738_NBNZ and 738_NB were not tested for the same reason. The creep strain curves show that for both test conditions, the 738_STD alloy has a longer

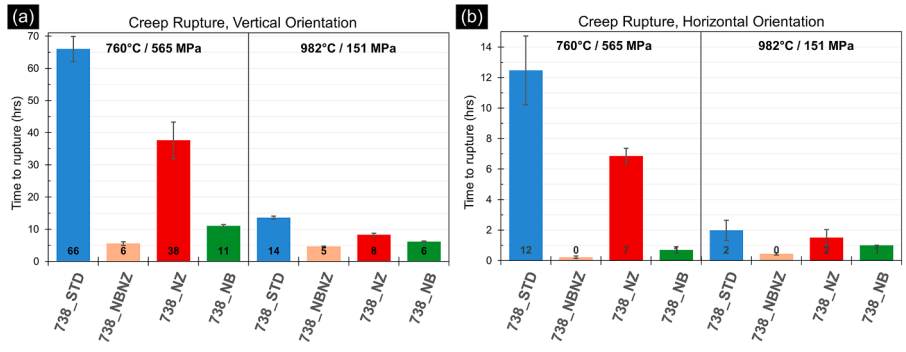

Fig. 15. Creep rupture life of the four alloys at 765°C / 565 MPa and 982°C / 151 MPa in the (a) Vertical orientation; and (b) horizontal orientation.

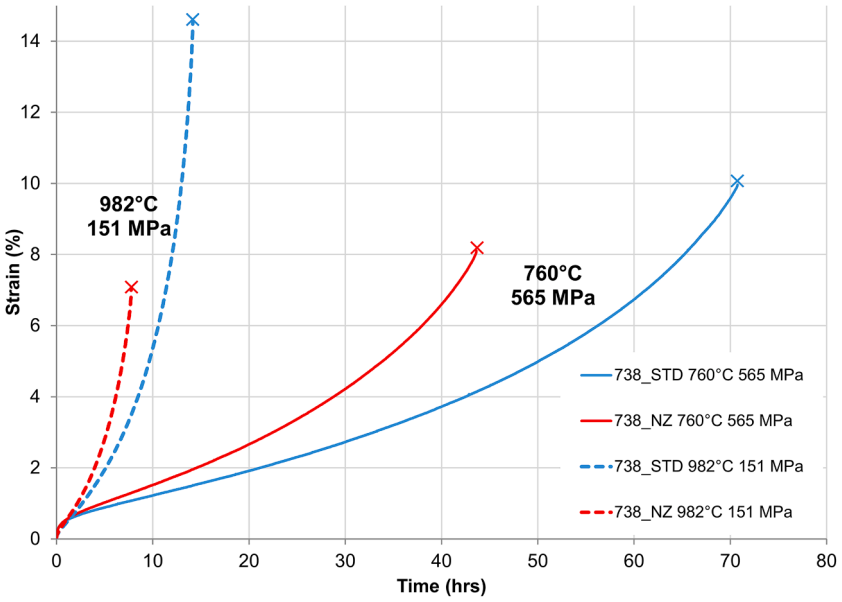

Fig. 16. Creep strain curves for vertical specimens of the 738_STD and 738_NZ alloys at 760°C / 565 MPa and 982°C / 151 MPa.

rupture life, with more creep ductility. Differences in minimum creep rate were also observed. At 760°C / 565 MPa, the 738_STD had a minimum creep rate of 1.2×10^{-3} s^{-1} whereas the rate for 738_NZ was measured to be 1.7×10^{-3} s^{-1}. At 982°C / 151 MPa, the 738_STD had a creep rate of 6.1×10^{-3} s^{-1} while the 738_NZ was 7.4×10^{-3} s^{-1}.

Uniaxial tensile tests were also performed with duplicate samples at 750°C and 980°C, in both vertical and horizontal orientations. The results in terms of yield strength, ultimate tensile strength, elongation after fracture, and reduction in area are summarized in Fig. 17.

In terms of yield strength and ultimate tensile strength, the 738_STD and 738_NZ alloys showed slightly higher values in both vertical and horizontal orientations compared to the 738_NBNZ and 738_NZ alloy variants. This was valid for both test temperatures. The differences are more obvious in ultimate tensile strength than in yield strength. Between 738_STD and 738_NZ, the differences in strength were not large enough to form any clear distinction.

The tensile ductility measurements showed that vertical samples had high ductility compared to horizontal samples. Tensile ductility was highest for 738_STD, and slightly lower for 738_NZ. A significantly lower ductility was noted for the 738_NBNZ and 738_NB alloys at both test

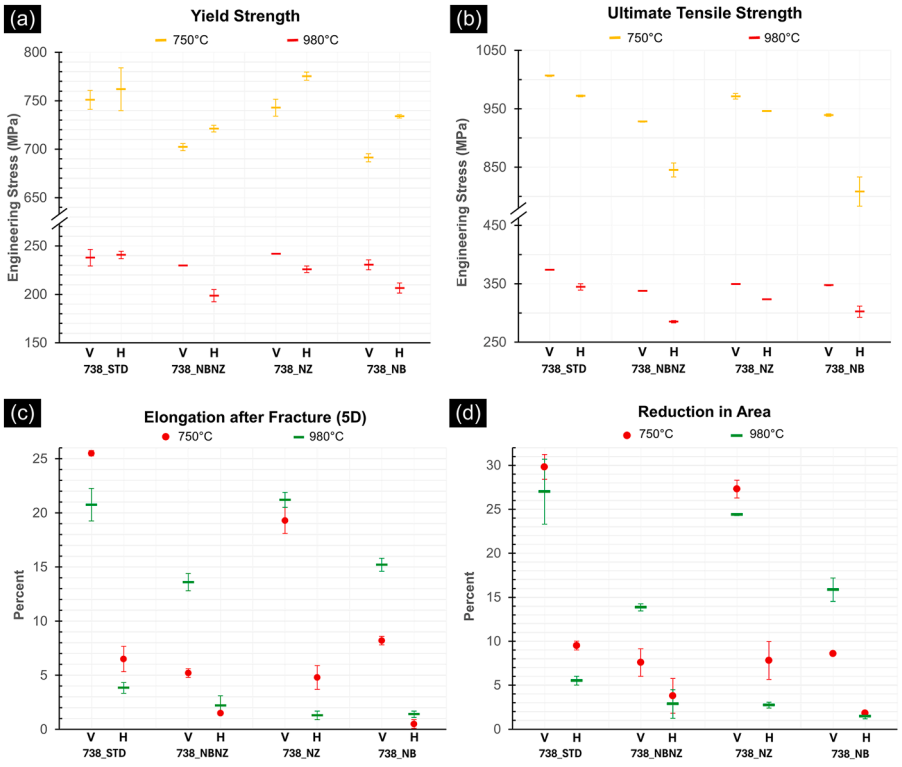

Fig. 17. Tensile properties of the four alloys in vertical and horizontal orientations at 750°C and 980°C: (a) yield strength; (b) ultimate tensile strength; (c) elongation after fracture; (d) reduction in area.

temperatures compared to the other alloys. For example, while 738_NZ showed 19% elongation after fraction at 750°C in the vertical orientation, the 738_NB alloy showed only 8%. In the horizontal orientation the 738_NB alloy showed very brittle fracture, only 0.5% elongation after fracture at 750°C, whereas the 738_NZ alloy showed 5% elongation at the same test condition. These results clearly demonstrate a loss of tensile ductility in the 738_NBNZ and 738_NB alloys. Between 738_STD and 738_NZ, it is notable that if only horizontal orientations are compared, the 738_STD alloy shows slightly more ductile behaviour in tensile deformation.

4. Discussion

4.1. Effects of B and Zr on processability and microcracking

Susceptibility to solidification cracking is known to be a function of two main factors: (1) the existence of a crack susceptible microstructure particularly one where liquid films are present; and (2) high levels of restraint or strain during solidification.

The results from microcracking assessment in Section 3.1 suggest that 738_STD, having both B and Zr, is the alloy most susceptible to microcracks. This is likely due to the well-known effect of B and Zr in segregating to and stabilizing the liquid [20,24,25]. Moreover, B and Zr have a cumulative effect when they are alloyed together, and have been reported to enhance the severity of segregation of other elements to the liquid, resulting in hot tearing and weld hot cracking [26–30]. The formation of liquid films at solidification grain boundaries in the last stage of freezing is known to be critical for solidification cracking, whereas increasing amounts of isothermally solidifying liquid do not typically exacerbate cracking [31]. This condition of liquid film formation is clearly met for 738_STD, as suggested by sharp gradient of the T vs $f_s^{\frac{1}{2}}$ curves seen in Fig. 3 and the large value of SCI. The other precondition for solidification cracking, i.e. strain, is satisfied for 738_STD (and all other variants) due to the high residual stress present in the as-built condition which is well known for PBF-LB [32–34]. However, a very large solidification temperature range, as determined for 738_STD in Section 3.1, compounds this effect because solidification shrinkage and thermal contraction act over a larger range of temperature, further exacerbating the negative impact of restraint.

The alloys 738_NZ and 738_NB, with only one of either B or Zr, show significantly reduced microcracking tendency, which is likely due to the decrease in extent of liquid film formation. While both B and Zr are known to segregate to the liquid, even when the other is absent (which explains why there is still some microcracking susceptibility in both 738_NB and 738_NZ), the possibility of liquid film formation at solidification grain boundaries is expected to be strongly reduced relative to their combined effect in 738_STD. This is supported by the Scheil curves and SCI values in Section 3.1. The finding of no microcracking susceptibility in 738_NBNZ, which included neither B nor Zr, again highlights the critical impact of these elements on creating the preconditions needed for microcracking to occur.

The trend of B and Zr content promoting microcracking (on their own and especially in combination) appears to be well supported when comparing the current results to the recent literature on PBF-LB of IN738LC. Vilanova et al. compared the cracking susceptibility of two IN738LC powders, one having both Zr and B within standard ranges (similar to 738_STD), and the other with Zr content in the normal range but very low B (akin to 738_NB). They found that the alloy with lowered B content was easier to process without microcracking [19]. Guo et al. performed a similar set of experiments with high and low B content alloys while holding the Zr content constant, resulting in higher crack density for the high B alloy [35]. Gruber et al. used a matrix of four alloys to systematically vary the B and Zr content (differing from the current matrix in that B and Zr levels were above of the standard alloy limits) and their results showed that the confluence of high B and Zr led to the highest levels of cracking, whereas cracks were less frequent when either B or Zr were low, and nearly no cracks formed when both elements were low [5]. Gruber et al. also concluded that the effect of only B on microcracking was stronger than the effect of only Zr. However, this is not reflected in the current results, likely due to the B contents used by Gruber et al. being above the standard alloy's upper limit in their experiments. Gruber et al. also emphasized the importance of powder properties, specifically powder surface chemical composition, not covered in this study, that can provide further explanation towards cracking susceptibility. Several researchers have also correlated the microcracking to Si which is another melting point depressant, however the Si contents in those alloys reportedly showing severe microcracking were generally much higher than those in the current study [36–38].

A number of studies have shown that the PBF-LB processing parameters also have an effect on microcracking, with higher energy input levels generally being shown as provoking microcracks [4,39]. It has also been shown that limiting the energy input by reducing laser power or increasing scanning speed can mitigate microcracking [40–42] however these results are limited to monolithic specimen geometries like cubes. In real AM builds, thermal conditions may vary greatly due to geometric effects and heat sink variation, rendering process parameter optimization less effective in cracking mitigation. By using relatively high energy input parameters, the current experimental results represent a worst-case scenario for cracking susceptibility of the alloy variants.

4.2. Scheil model and cracking index

While the Scheil solidification simulations with solute trapping and the SCI values calculated thereof are in support of the experimental microcracking results, some critical assessment on their interpretation is required. The Scheil model with solute trapping is clearly an improvement over the classic Scheil model for simulating rapid solidification conditions, however solute trapping is currently considered only in the primary phase, i.e. the γ matrix, whereas other phases follow the classic Scheil model. In reality, solute elements are also trapped in other phases, such as the MC carbides, as revealed by Atom Prode Tomography (APT) analysis of as-built IN738LC by Lindgren et al. [6]. This implies that the Scheil model with solute trapping may be overestimating segregation of solutes in the later stages of solidification. On the other hand, the Scheil model is idealised so that it does not consider grain boundary misorientation when modelling segregation. Microcracks in PBF-LB superalloys have been shown to occur more frequently at grain boundaries with higher misorientation [5,35], and solutes such as B have also been detected at higher concentrations in high angle boundaries [43], therefore in this aspect segregation may be underestimated by the Scheil model.

The selection of phases allowed to form is also a critical input for the Scheil simulation, as phase formation influences the availability of solutes in the liquid as the simulation progresses. As mentioned in Section 2, the model was restricted to only the liquid, γ, γ′, and MX carbonitride phases. Note that γ′ has not been excluded from the calculation as there are validated reports of γ′ precursors forming in as-built IN738LC [6,44,45], and since only a 0.025 volume fraction of γ′ is formed according to the simulation, and the phase consumes no B or Zr, the inclusion of this phase is unlikely to significantly affect the results. Other phases formed may be more critical. By default, the Thermo-Calc 2025a software with the TCNI12 database includes other phases in the calculation based on their thermodynamic stability, including M_2B and MB_2 borides and the intermetallic η phase (called M2B_TETR, MB2_C32 and NI3TI_D024 in Thermo-Calc respectively). While there are reports of nano-sized boron enrichments at interdendritic regions in IN738LC by APT [6,14] and by TEM [35], these have not been crystallographically verified to be borides. B is also included as a component in the MX carbonitride in the TCNI12 database, which further justifies exclusion of borides from the calculation. The η phase has not been reported in the as-built microstructure of IN738LC, and is unlikely to form due to the low Ti to Al ratio

in the alloy, nor is it predicted to be thermodynamically stable at equilibrium by Thermo-Calc [11]. Had η formed in the as-built microstructure, it would likely be coarsened after sub-solvus solution heat treatment, as was shown for IN939 [46]. These factors justify its exclusion from the calculation. Moreover, calculating the SCI for the four alloy variants with the inclusion of M2B_TETR, MB2_C32 and NI3TI_D024 results in values of 7890, 6300, 7577, and 6771 for 738_STD, 738_NBNZ, 738_NZ, and 738_NB respectively, an outcome which still agrees with the trend seen in the experimental microcracking susceptibility results. The corresponding Scheil and SCI curves can be seen in Appendix Fig. A3. The selection of phases, in addition to the use of the solute trapping model, is likely to be a reason for the discrepancy in the SCI values for IN738LC determined by others [47,48] and those in the current results.

While Kou's SCI model itself is shown to be highly applicable to the AM of Ni-base superalloys [47] there are aspects specific to alloy systems which are not considered in the model. The formation of primary phases at the end of solidification may act as sites for heterogenous nucleation in the solidification of following layers [49] or may also act as crack nucleation sites in case they are brittle in nature. In the case of IN738LC, where MC carbides are the only major product of the solidification after the γ phase, this factor is unlikely to affect the reliability of the model.

4.3. Effects of B and Zr on the heat treated microstructure

The results in Section 3.2 show that the inclusion or exclusion of B and / or Zr from the composition of PBF-LB IN738LC have a noticeable effect on the microstructure. The intention of the experimental setup was to hold all other parameters constant, including PBF-LB processing, HIP, and heat treatment, with the only variation being the B and Zr content.

From the characterization of the grain boundary microstructures, it can be deduced that B alloying caused the formation of the lamellar grain boundary phases seen in Fig. 9 (a), Fig. 9 (c), Fig. 10 and Fig. 13 (a), because these phases were absent from the microstructures of the 738_NBNZ and 738_NB alloys. The Cr-rich composition of these lamellar phases, and detection of C content, suggest that these can be either $M_{23}(C,B)_6$ phases, which have been reported previously in PBF-LB IN738LC [50], cast IN738LC [51], and several other superalloys [52–56], or other borocarbide phases. However, the exact phase could not be conclusively identified, and the possibility of the formation of M_5B_3 and M_3B_2 borides, which are also Cr-rich and are often reported in IN738LC [25,57], cannot be excluded. Similarly, the sub-micron sized B-rich precipitates seen by NanoSIMS maps in 738_STD and by EDX in 738_NZ are likely to be borides or $M_{23}C_6$ carbides with B dissolved or present at the carbide-matrix interface. Overall, the evidence suggests that B is found at the grain boundary region in both of the variants in which it is alloyed, either in solid solution or in the form of carbide or boride precipitates.

Note that Thermo-Calc predicts $M_{23}C_6$ as a stable phase in all the alloy variants (see Table 5), however, no B content is predicted in the phase. M_2B is also predicted which has been reported in cast IN738LC [58] but M_5B_3 and M_3B_2 are not predicted. This discrepancy is likely due to the thermodynamic equilibrium nature of the simulation, whereas the microstructure in the experiment includes metastable phases.

While Zr could be identified in the microstructures of both 738_STD and 738_NB alloys, its effect on the microstructure was not very apparent. Zr has high affinity for oxygen, which is typically available in up to 1000 ppm levels during PBF-LB processing, and would likely form ZrO_2 in-process or during heat treatment. The presence of this phase could explain the discrete particles of Zr seen within grains in NanoSIMS and SEM-EDX. While this could not be confirmed experimentally, others have also reported presence of ZrO_2 in PBF-LB superalloys after heat treatment [59]. For instances where Zr was detected together with C and/or B in discrete particles, a plausible structure is that of ZrC, which has been reported in several alloys including IN738LC [52,56,60–62], or MC carbide with both Zr and B, as reported in IN939 [54]. Theska et al. reported the co-precipitation of the M_2B boride phase on ZrO_2 particles, which may explain the colocation of Zr and B seen in the NanoSIMS maps for 738_STD. Additionally, Gruber et al. have reported formation of ZrB_2 and its further oxidation to ZrO_2 and B_2O_3, hence explaining the co-existence of Zr and B and related oxides, also confirmed by thermodynamic calculations [5]. According to the literature on cast Ni-base superalloys, Zr is often found in sulphides and sulpho-carbides [13,63]. This could not be ascertained in the experimental work as detection of ppm levels of sulphur is extremely challenging with the utilized characterization methods.

The effect of B and Zr on the grain structure was captured well by EBSD analysis, as described in section 3.3. All the alloy variants underwent the same heat treatment procedure, however, the B-bearing alloys produced a much lower frequency of CSL boundaries, especially Σ3 boundaries, and a slightly higher frequency of low angle grain boundaries. The reduced frequency of twin boundaries is explained by the reported solute drag effect of B at grain boundaries. Twins are believed to form by the interaction of migrating grain boundaries with stacking faults. B presence at grain boundaries reduces boundary mobility in the 738_STD and 738_NZ alloys, thus preventing the formation of twins in those alloys. By the same reasoning, in 738_NBNZ and 738_NB, where B is absent, grain boundaries would be more mobile and prone to migration and growth accidents, forming the twins observed in Fig. 6 and Fig. 8. Thuvander et al. and Chiu et al. have also reported on the ability of B alloying to inhibit grain growth in Ni-alloys [64,65]. Pande et al. also showed that small B additions can drastically reduce twin density due to reduced grain boundary migration [66]. Note that 738_NB showed a lower frequency of CSL boundary formation than 738_NBNZ, suggesting that Zr alloying also played a role in inhibiting grain boundary mobility. This may be expected especially if the microstructure contained ZrC or ZrO_2, which would have a strong Zener pinning effect if they were present.

The higher frequency of low angle boundaries in 738_STD and 738_NZ may potentially be explained by the recent report from Antonov et al. of B trapping at dislocations in a Ni-base superalloy, observed by APT. B was found at tubular shaped structures both in the as-built condition and after a sub-solvus heat treatment, and was deemed to have stabilized these dislocations [67]. Dislocation movement is required for annealing of low-angle grain boundaries, and dislocation stabilization by B could explain why higher frequencies of low angle boundaries were observed only for the B-bearing alloys in the current results. To the best of the authors' knowledge, this effect of minor element content on grain boundary character in PBF-LB IN738LC after heat treatment has not been reported before. However, further characterisation is needed to experimentally link this effect in PBF-LB processed IN738LC variants with B content.

Table 5
Volume fractions of various phases predicted by Thermo-Calc 2025a for the four alloys at 850°C and 1120°C at equilibrium.

	850°C						1120°C					
	MC	$M_{23}C_6$	M_2B	MB_2	γ	γ′	MC	$M_{23}C_6$	M_2B	MB_2	γ	γ′
738_STD	-	2.0	0.2	-	52	45	0.8	-	-	0.07	91	8
738_NBNZ	-	2.0	-	-	54	44	0.8	-	-	-	94	5
738_NZ	-	2.2	0.2	-	55	43	0.9	-	-	0.05	96	3
738_NB	-	2.4	-	-	54	43	1.0	-	-	-	96	4

4.4. Effects of B and Zr on mechanical performance

The results in Section 3.3 clearly show that 738_STD and 738_NZ produce significantly better mechanical performance in terms of creep rupture life and elevated temperature tensile strength and ductility compared to 738_NBNZ and 738_NB. Since the grain size and γ' precipitate size and fraction are very similar between all the alloys, this trend can be attributed to the effects of B in the composition. B has been reported to segregate to and enhance grain boundary cohesivity by forming covalent bonds with metallic elements [68]. Alternately it has been credited with retarding creep by slowing down grain boundary diffusion through eliminating vacancies [69], and preventing agglomeration of grain boundary carbides and γ' [70]. It has also been suggested that B enhances grain boundary ductility by easing dislocation movement across grain boundaries [71]. While the exact mechanism of grain boundary strength enhancement by B is still debated, its presence at grain boundaries and beneficial effects are clearly recognized and widely utilised in many superalloys [20,56].

The beneficial effect of Zr was evident from the fact that 738_STD showed better rupture life than 738_NZ, and also from the marginally higher rupture life of 738_NB over 738_NBNZ. While the mechanism by which Zr provided some benefit is not clear from the microstructure characterization, the evidently lower grain boundary mobility of 738_NB versus 738_NBNZ seen from EBSD measurements is plausible as a contributory factor. Other factors could be related to the reported influences of Zr in stabilising carbides thereby preventing brittle carbide film formation at grain boundaries, though such effects are unlikely to manifest at the short rupture lives observed in the current set of results [56,72,73].

The stark difference in performance with and without B is not surprising, since similar trends have been reported in the literature for numerous superalloys, where omission of B from the composition greatly diminishes creep performance [25,69,74,75] and negatively affects tensile ductility [71,76]. For AM superalloys, Dörries et al. have found the same trend in a novel high-Ta superalloy, where omission of B and Zr rendered the alloy so brittle that mechanical testing could not be satisfactorily completed [77]. Després et al. also found null creep performance when both Zr and B were removed from PBF-LB AD730 [78].

When discussing mechanical properties, it must be acknowledged that even the highest creep life shown in the current results is far below the typical creep rupture life of cast IN738LC. At 982°C and 151 MPa the cast alloy has life usually above 30 h [3] (highest result for 738_STD was 15 h in vertical) and at 760°C and 565 MPa the cast alloy would not be expected to rupture earlier than 200 h (highest result for 738_STD was 70 h in vertical orientation) [79]. The large anisotropy and underperformance in the horizontal orientation is a further challenge, which is likely due to the strong texture and small grain size of the PBF-LB alloys, especially in the XY plane [9,11]. Additionally, recent research by Kianinejad et al. has suggested that activation of microtwinning deformation mechanisms can also explain the orientation dependent creep behaviour, at least for creep at temperatures at or below 850°C [80].

Note that in the current experimental regime, the sub-solvus solution heat treatment from cast IN738LC was kept as a constant in order to ensure comparability between the alloys, however this heat treatment is not designed for the fine grained PBF-LB microstructure. Owing to the small grain size from PBF-LB, grain boundary area is increased by at least an order of magnitude compared to cast [81]. Assuming the increased frequency of low angle grain boundaries in 738_STD and 738_NZ is due to the trapping of B at dislocations, this also implies that even less B is available at high angle grain boundaries for strengthening, potentially contributing to the generally low creep performance relative to cast IN738LC. A super-solvus heat treatment as tested by Messe et al. or Song et al. may be a good solution in this regard [11,50] and may also help to reduce the anisotropy, as demonstrated for other alloys [81]. Alternatively, the grain boundary strengthener content may be tailored for grain size, i.e. more of B and Zr should be added with finer grain size, as is recommended for various fine grained powder metallurgy superalloys [75,82].

As previously discussed in Section 3.3, the application of HIP to heal microcracks in all mechanical testing samples was important to ensure comparability between alloy variants regardless of as-built crack density. This naturally raises the question that if HIP can be employed to heal cracks, why is crack-free processing necessary? While it is true that microcracks in the interior of specimens can be healed by HIP, microcracks which are open to the surface cannot be healed, nor can structures with excessively large or inter-connected microcracks [83]. Furthermore, unlike the simple specimen geometries used in the work (see Fig. 1), real parts manufactured by PBF-LB from IN738LC are likely to have complex geometrical features including thin walls and overhangs, which may exacerbate microcracking especially in the surface and near-surface regions [84,85]. Microcracks in such geometries cannot be healed by HIP, therefore crack-free processing remains an important goal despite the crack-healing possibilities of HIP.

4.5. Implications and outlook

The trend in mechanical behaviour suggests that both B and Zr must be included in the composition of PBF-LB IN738LC for optimum high temperature properties. However, the cracking susceptibility results show that alloying both these elements would also result in severe microcracking in PBF-LB processing. A possible solution to this conundrum could be the exclusion of Zr from the composition, as previously suggested for other alloys [78,86], but according to the current results this would necessitate a compromise on creep performance.

It is plausible based on the above discussion that with re-designed heat treatment the creep properties of 738_NZ could be improved to some extent with relatively low microcracking. An alternative approach, however, could be to alloy additional liquid segregating solutes to mitigate cracking by “eutectic healing” at the end of solidification, as is known from the welding metallurgy of Al-alloys [31]. An addition of grain boundary strengthening solutes could also be useful in improving the creep performance of the fine-grained microstructure.

5. Conclusions

An investigation was conducted into the PBF-LB processing, microcracking susceptibility, microstructure development, and mechanical properties of four variants of IN738LC: the standard composition (738_STD) having both B and Zr in the typical range; a variant (738_NBNZ) where both B and Zr were absent from the composition; a variant (738_NZ) with only B alloying and absence of Zr; and a variant (738_NB), with only Zr alloying and absence of B.

The results show that when B and Zr are present in the composition together, a high cracking density of 0.76 mm/mm^2 is produced. When only one of B or Zr is in the composition, the density of microcracks drops to 0.02 mm/mm^2. When neither B nor Zr are alloyed, no microcracks were found.

After a sub-solvus solution heat treatment at 1120°C (including HIP) and an ageing heat treatment at 850°C, a fine grained and heavily cube textured microstructure was developed in all variants. B could be detected in a Cr-rich lamellar phase at grain boundaries in both the B-bearing alloys. In the alloys without B only grain boundary carbides were observed. Importantly, the 738_NBNZ alloy showed small twin boundaries in 36% of grains in its microstructure. The 738_NB alloy was

also found to have twins in ≈20% of its grains, whereas the B-bearing alloys had very low twin fractions of less than 2%. These observations suggest that omission of B has a particularly strong effect (more than Zr) on increasing grain boundary mobility.

Uniaxial tensile tests at 750°C and 980°C revealed relatively low ductility for the 738_NBNZ and 738_NB alloys, confirming the understanding that B is critical for high temperature ductility. Creep rupture testing with loading parallel to the build direction at 760°C and 565 MPa revealed the highest rupture life and lowest creep rate for 738_STD. Omission of Zr reduced the rupture life by a factor of 2, and omission of B reduced it by a factor of 11. Similar trends were also observed for creep tests at 982°C and 151 MPa, indicating clearly that omission of B severely degrades creep performance, and that omission of Zr also has a negative effect.

The results indicate that microcrack-free processing and optimum creep performance are conflicting requirements for PBF-LB processed IN738LC, and alternative processing, post-processing, and alloy design strategies may be needed to successfully address this issue.

Data availability

The raw/processed data required to reproduce these findings cannot be shared at this time due to legal or ethical reasons.

CRediT authorship contribution statement

Abdul Shaafi Shaikh: Writing – original draft, Visualization, Investigation, Formal analysis, Data curation, Conceptualization. **Bharat Mehta:** Writing – review & editing, Validation, Software, Investigation, Formal analysis, Data curation. **Yiming Yao:** Visualization, Investigation, Formal analysis. **Eduard Hryha:** Writing – review & editing, Validation, Supervision, Resources, Project administration, Funding acquisition, Formal analysis, Conceptualization.

Declaration of competing interest

The authors declare that they have no known competing financial interests or personal relationships that could have appeared to influence the work reported in this paper.

Acknowledgements

This work was performed in the framework of the Centre for Additive Manufacturing – Metal (CAM^2), financed by Vinnova. Johannes Gårdstam of Quintus Technologies is gratefully acknowledged for performing the HIP. The authors would like to thank Dr. Elias Ranjbari for his help with the NanoSIMS analysis.

Appendix

Fig. A1, Fig. A2, Fig. A3, Fig. A4, Table A1

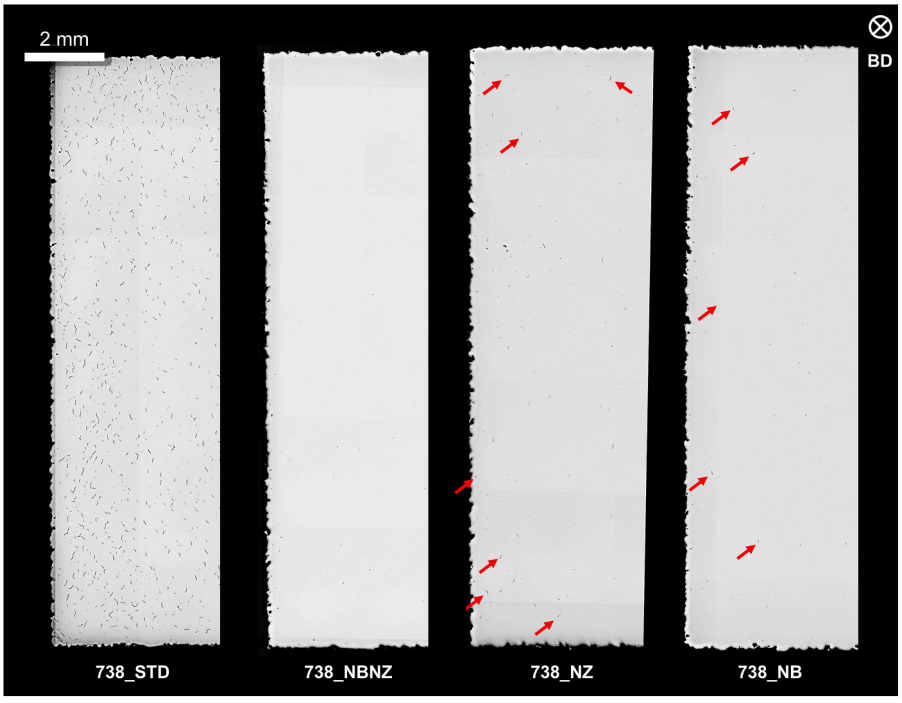

Fig. A1. Overview optical micrographs of plain polished XY cross-sections of all 4 alloys in the as-built condition, showing the difference in microcracking between variants. Red arrows point to cracks in the 738_NZ and 738_NB alloys.

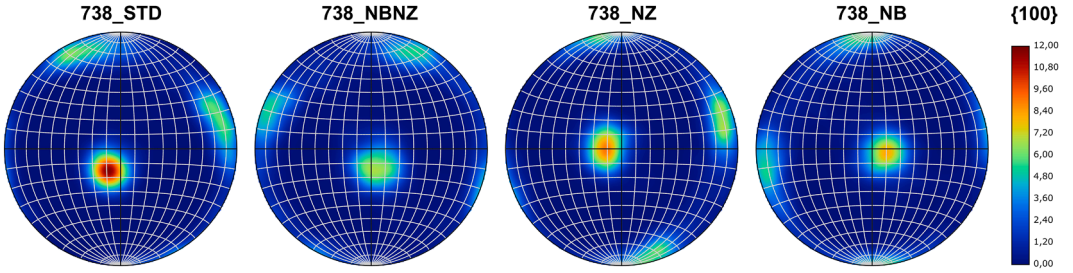

Fig. A2. (100) pole figures obtained from EBSD measurements for the 4 alloys after heat treatment. The centre of the pole figure is oriented parallel to the building direction.

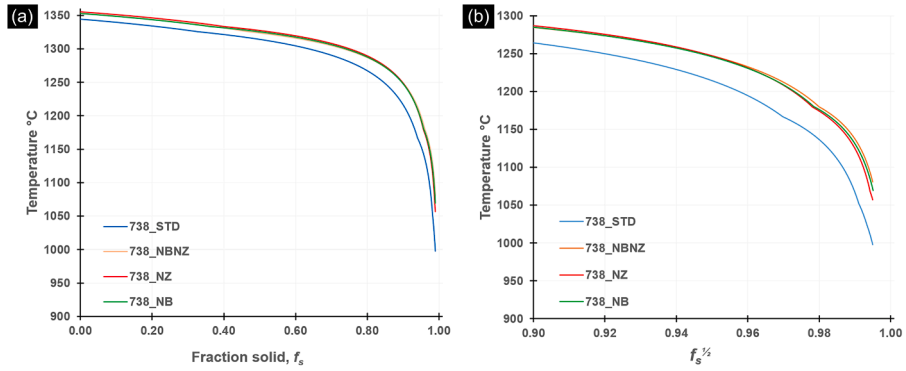

Fig. A3. (a) Temperature vs fraction solid f_s for the four alloys from Scheil solidification simulations with solute trapping using Thermo-Calc 2025a; (b) Temperature vs $f_s^{½}$ curves ($f_s^{½}$ = 0.9-1.0) for the 4 alloys used for calculating the Kou Solidification Cracking Index. The calculations differ from those in Fig. 3 in that the NI3TI_D024, MB2_C32, and M2B_TETR phases were not excluded from the calculation.

Table A1
Detailed results of creep rupture testing.

Condition	Orientation	Test temperature °C	Applied Stress MPa	Rupture Life hrs			Elongation at rupture (4D) %			Reduction in area %		
738_STD	Vertical	760	565	66.0	±	3.9	10.5	±	1.5	15.6	±	0.6
	Horizontal	760	565	12.5	±	2.3	2.3	±	0.3	6.9	±	1.0
738_NBNZ	Vertical	760	565	5.6	±	0.6	3.5	±	0.5	7.6	±	0.6
	Horizontal	760	565	0.2	±	0.1	0.9	±	0.6	4.7	±	1.3
738_NZ	Vertical	760	565	37.6	±	5.7	9.3	±	0.5	13.4	±	0.4
	Horizontal	760	565	6.9	±	0.5	2.3	±	0.2	5.6	±	0.5
738_NB	Vertical	760	565	11.1	±	0.4	4.7	±	0.3	11.0	±	1.0
	Horizontal	760	565	0.7	±	0.2	1.3	±	0.2	6.0	±	1.0
738_STD	Vertical	982	151	13.6	±	0.4	15.0	±	0.1	17.7	±	1.9
	Horizontal	982	151	2.0	±	0.7	6.7	±	2.6	7.4	±	3.7
738_NBNZ	Vertical	982	151	4.6	±	0.1	10.8	±	1.9	10.4	±	2.4
	Horizontal	982	151	0.4	±	0.1	3.9	±	1.0	5.3	±	2.4
738_NZ	Vertical	982	151	8.3	±	0.5	10.0	±	1.6	10.6	±	3.4
	Horizontal	982	151	1.5	±	0.5	4.8	±	0.3	5.5	±	2.0
738_NB	Vertical	982	151	6.2	±	0.2	15.5	±	0.5	14.5	±	0.5
	Horizontal	982	151	1.0	±	0.0	7.5	±	0.5	10.5	±	0.5

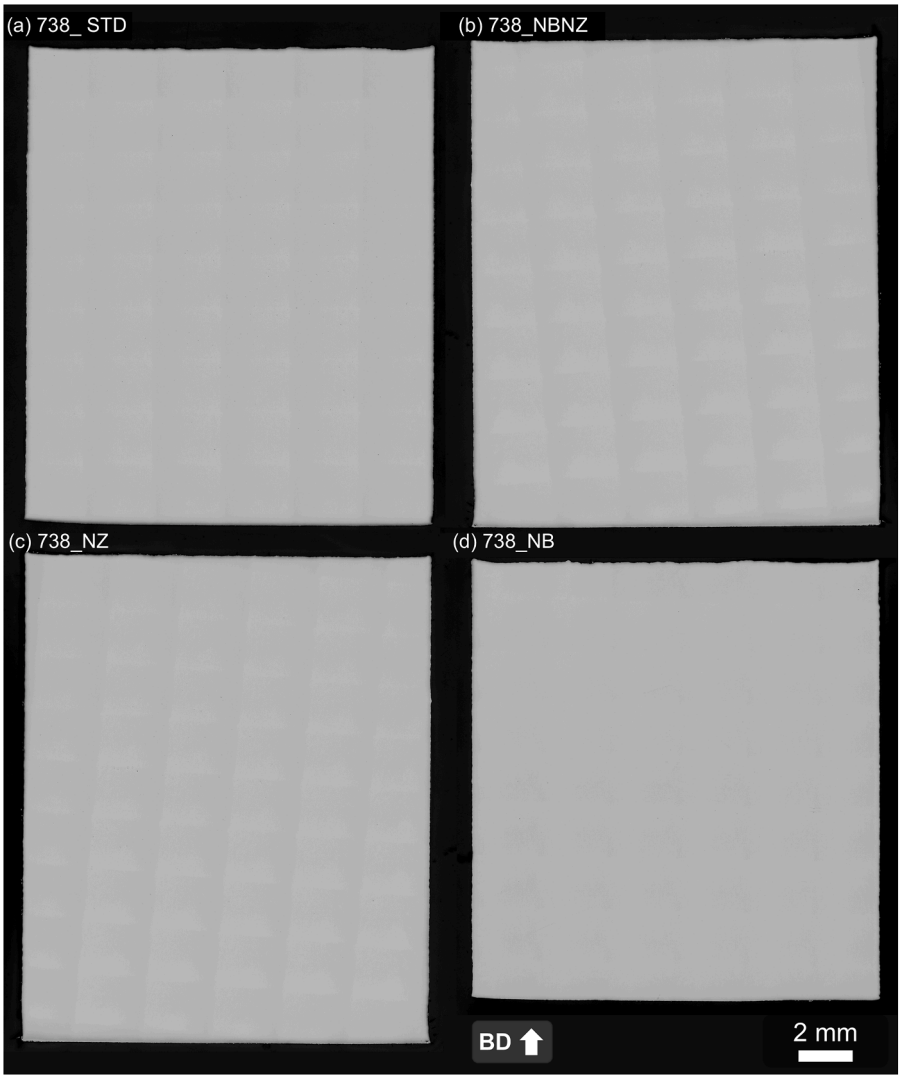

Fig. A4. Overview optical micrographs of plain polished cross-sections of all 4 alloys in the HIP and heat treated condition.

References

[1] N. Kwabena Adomako, N. Haghdadi, S. Primig, Electron and laser-based additive manufacturing of Ni-based superalloys: a review of heterogeneities in microstructure and mechanical properties, Mater. Des. 223 (2022) 111245, https://doi.org/10.1016/j.matdes.2022.111245.

[2] The International Nickel Company, Alloy IN-738 technical data.

[3] AMS F Corrosion and Heat Resistant Alloys Committee, AMS5410C (2017) Nickel alloy, corrosion- and heat resistant, investment castings: 61Ni - 16Cr - 8.5Co - 1.8Mo - 2.6W - 0.85Cb (Nb) - 3.4Ti - 1.8Ta - 3.4Al - 0.010B - 0.05***Zr***, Vacuum Melted, Vacuum Cast, As Cast, or Solution Treated, or Solution and Precipitation Hardened, SAE International, 400 Commonwealth Drive, Warrendale, PA, United States.

[4] M. Cloots, P.J. Uggowitzer, K. Wegener, Investigations on the microstructure and crack formation of IN738LC samples processed by selective laser melting using gaussian and doughnut profiles, Mater. Des. 89 (2016) 770–784, https://doi.org/10.1016/j.matdes.2015.10.027.

[5] H. Gruber, E. Hryha, K. Lindgren, Y. Cao, M. Rashidi, L. Nyborg, The effect of boron and zirconium on the microcracking susceptibility of IN-738LC derivatives in laser powder bed fusion, Appl. Surf. Sci. 573 (2022) 151541, https://doi.org/10.1016/j.apsusc.2021.151541.

[6] K. Lindgren, F. Schulz, H. Gruber, A. Markström, E. Hryha, On the role of Zr and B addition on solidification cracking of IN738LC produced by laser powder bed fusion, Materialia 26 (2022) 101609, https://doi.org/10.1016/j.mtla.2022.101609.

[7] G.M. Volpato, U. Tetzlaff, M.C. Fredel, A comprehensive literature review on laser powder bed fusion of inconel superalloys, Addit. Manuf. 55 (2022) 102871, https://doi.org/10.1016/j.addma.2022.102871.

[8] L. Rickenbacher, T. Etter, S. Hövel, K. Wegener, High temperature material properties of IN738LC processed by selective laser melting (SLM) technology, Rapid Prototyp, Journal 19 (2013) 282–290.

[9] K. Kunze, T. Etter, J. Grässlin, V. Shklover, Texture, anisotropy in microstructure and mechanical properties of IN738LC alloy processed by selective laser melting (SLM), Mater. Sci. Eng. A 620 (2015) 213–222, https://doi.org/10.1016/j.msea.2014.10.003.

[10] J. Wilkes, K. Hoopes, J. Helfand, Creep and tensile properties of DMLS Inconel 738LC coupons and comparison to cast properties, in: The 6th International Supercritical CO2 Power Cycles Symposium, 2018.

[11] H.Y. Song, M.C. Lam, Y. Chen, S. Wu, P.D. Hodgson, X.H. Wu, Y.M. Zhu, A. J. Huang, Towards creep property improvement of selective laser melted Ni-based superalloy IN738LC, J. Mater. Sci. Technol. 112 (2022) 301–314, https://doi.org/10.1016/j.jmst.2021.09.050.

[12] M. McLean, A. Strang, Effects of trace elements on mechanical properties of superalloys, Met. Technol. 11 (1984) 454–464, https://doi.org/10.1179/030716984803274800.

[13] B. Geddes, H. Leon, X. Huang, Superalloys: Alloying and performance, ASM International, Materials Park Ohio, 2010.

[14] E.A. Jägle, Z. Sheng, L. Wu, L. Lu, J. Risse, A. Weisheit, D. Raabe, Precipitation reactions in age-hardenable alloys during laser additive manufacturing, JOM 68 (2016) 943–949, https://doi.org/10.1007/s11837-015-1764-2.

[15] S. Kou, A criterion for cracking during solidification, Acta Mater. 88 (2015) 366–374, https://doi.org/10.1016/j.actamat.2015.01.034.

[16] D.A. Porter, K.E. Easterling, M.Y. Sherif, Phase Transformations in Metals and Alloys, CRC Press, Boca Raton, 2021.

[17] M.J. Aziz, Model for solute redistribution during rapid solidification, J. Appl. Phys. 53 (1982) 1158–1168, https://doi.org/10.1063/1.329867.

[18] M.J. Aziz, T. Kaplan, Continuous growth model for interface motion during alloy solidification, Acta Metall. 36 (1988) 2335–2347, https://doi.org/10.1016/0001-6160(88)90333-1.

[19] M. Vilanova, M.C. Taboada, A. Martinez-Amesti, A. Niklas, M. San Sebastian, T. Guraya, Influence of Minor alloying element additions on the crack susceptibility of a nickel based superalloy manufactured by LPBF, Materials 14 (2021) 5702, https://doi.org/10.3390/ma14195702.

[20] C.T. Sims, N.S. Stoloff, W.C. Hagel, Superalloys II: High-Temperature Materials for Aerospace and Industrial Power, Wiley, New York, USA, 1987.

[21] H.R. Zhang, O.A. Ojo, M.C. Chaturvedi, Nanosize boride particles in heat-treated nickel base superalloys, Scr. Mater. 58 (2008) 167–170, https://doi.org/10.1016/j.scriptamat.2007.09.049.

[22] F. Theska, R.F. Webster, S.R. Street, M. Lison-Pick, S. Primig, Co-precipitation of M2B on ZrO2 in a Ni-base superalloy with B & Zr additions, Mater. Chem. Phys. 310 (2023) 128466, https://doi.org/10.1016/j.matchemphys.2023.128466.

[23] A.S. Shaikh, F. Schulz, K. Minet-Lallemand, E. Hryha, Microstructure and mechanical properties of Haynes 282 superalloy produced by laser powder bed fusion, Mater. Today Commun. 26 (2021) 102038, https://doi.org/10.1016/j.mtcomm.2021.102038.

[24] F. Qi, L. Yu, G. Zhao, X. Xin, B. Zhang, W. Sun, Effect of Zr on solidification segregation behavior of K417G alloy and its anomalous effect during rapid cooling process, J. Alloys. Compd. 835 (2020) 155243, https://doi.org/10.1016/j.jallcom.2020.155243.

[25] H. Wang, J. Yang, J. Meng, S. Ci, Y. Yang, N. Sheng, Y. Zhou, X. Sun, Effects of B content on microstructure and high-temperature stress rupture properties of a high chromium polycrystalline nickel-based superalloy, J. Alloys. Compd. 860 (2021) 157929, https://doi.org/10.1016/j.jallcom.2020.157929.

[26] S.A. Hosseini, S.M. Abbasi, K.Z. Madar, The effect of boron and zirconium on the structure and tensile properties of the cast nickel-based superalloy ATI 718Plus, J. Mater. Eng. Perform. 27 (2018) 2815–2826, https://doi.org/10.1007/s11665-018-3372-0.

[27] D. Heydari, A.S. Fard, A. Bakhshi, J.M. Drezet, Hot tearing in polycrystalline Ni-based IN738LC superalloy: influence of Zr content, J. Mater. Process. Technol. 214 (2014) 681–687, https://doi.org/10.1016/j.jmatprotec.2013.10.001.

[28] H. Zhu, Y. Tang, Y. Li, Y. Zhu, Z. Hu, C. Shi, Effect of boron and zirconium on directional solidification behaviour and segregation of DS IN738 superalloy, Mater. High Temp. 10 (1992) 39–44, https://doi.org/10.1080/09603409.1992.11689396.

[29] J. Zhang, R.F. Singer, Effect of Zr and B on castability of Ni-based superalloy IN792, Met. Mater. Trans. A 35 (2004) 1337–1342, https://doi.org/10.1007/S11661-004-0308-0.

[30] J.N. DuPont, S.D. Kiser, J.C. Lippold, Welding Metallurgy and Weldability of Nickel-base Alloys, John Wiley & Sons, Hoboken, New Jersey, 2009.

[31] J.C. Lippold, Welding Metallurgy and Weldability, John Wiley & Sons Inc, Hoboken New Jersey, 2015.

[32] A. Martucci, G. Marchese, E. Bassini, M. Lombardi, Effects of stress-relieving temperature on residual stresses, microstructure and mechanical behaviour of Inconel 625 processed by PBF-LB/M, Metals 13 (2023) 796, https://doi.org/10.3390/met13040796.

[33] P. Pant, F. Salvemini, S. Proper, V. Luzin, K. Simonsson, S. Sjöström, S. Hosseini, R. L. Peng, J. Moverare, A study of the influence of novel scan strategies on residual stress and microstructure of L-shaped LPBF IN718 samples, Mater. Des. 214 (2022) 110386, https://doi.org/10.1016/j.matdes.2022.110386.

[34] A. Fardan, A. Fazi, R.L. Peng, T. Mishurova, M. Thuvander, G. Bruno, H. Brodin, E. Hryha, Fine-tuning melt pools and microstructures: taming cracks in powder bed fusion—Laser beam of a non-weldable Ni-base superalloy, Materialia 34 (2024) 102059, https://doi.org/10.1016/j.mtla.2024.102059.

[35] C. Guo, G. Li, F. Zhou, X. Li, Z. Xu, C. Liu, X. Hu, H. Lu, Z. Li, Q. Zhu, Understanding the significant effect of boron content on the printability of IN738LC superalloy fabricated using laser powder bed fusion, Opt. Laser. Technol. 159 (2023) 108954, https://doi.org/10.1016/j.optlastec.2022.108954.

[36] R. Engeli, T. Etter, S. Hövel, K. Wegener, Processability of different IN738LC powder batches by selective laser melting, J. Mater. Process. Technol. 229 (2016) 484–491, https://doi.org/10.1016/j.jmatprotec.2015.09.046.

[37] Z. Sun, Y. Ma, D. Ponge, S. Zaefferer, E.A. Jägle, B. Gault, A.D. Rollett, D. Raabe, Thermodynamics-guided alloy and process design for additive manufacturing, Nat. Commun. 13 (2022) 4361, https://doi.org/10.1038/s41467-022-31969-y.

[38] A. Hariharan, L. Lu, J. Risse, A. Kostka, B. Gault, E.A. Jägle, D. Raabe, Misorientation-dependent solute enrichment at interfaces and its contribution to defect formation mechanisms during laser additive manufacturing of superalloys, Phys. Rev. Mater. 3 (2019) 44s, https://doi.org/10.1103/PhysRevMaterials.3.123602.

[39] C. Guo, S. Li, S. Shi, X. Li, X. Hu, Q. Zhu, R.M. Ward, Effect of processing parameters on surface roughness, porosity and cracking of as-built IN738LC parts fabricated by laser powder bed fusion, J. Mater. Process. Technol. 285 (2020) 116788, https://doi.org/10.1016/j.jmatprotec.2020.116788.

[40] M. Vilanova, R. Escribano-García, T. Guraya, M.S. Sebastian, Optimizing laser powder bed fusion parameters for IN-738LC by response surface method, Materials 13 (2020), https://doi.org/10.3390/ma13214879.

[41] N. Perevoshchikova, J. Rigaud, Y. Sha, M. Heilmaier, B. Finnin, E. Labelle, X. Wu, Optimisation of selective laser melting parameters for the Ni-based superalloy IN-738 LC using Doehlert's design, Rapid. Prototyp. J. 23 (2017) 881–892, https://doi.org/10.1108/RPJ-04-2016-0063.

[42] D. Grange, J.D. Bartout, B. Macquaire, C. Colin, Processing a non-weldable nickel-base superalloy by Selective Laser Melting: role of the shape and size of the melt pools on solidification cracking, Materialia 12 (2020) 100686, https://doi.org/10.1016/j.mtla.2020.100686.

[43] Q.-Q. Ren, E.B. Raeker, K.M. Pusch, T.M. Pollock, S.A. Forsik, N. Zhou, A.D. Dicus, M.M. Kirka, J.D. Poplawsky, Understanding the influence of boron in additively manufactured GammaPrint®-700 CoNi-based superalloy, Addit. Manuf. 92 (2024) 104370, https://doi.org/10.1016/j.addma.2024.104370.

[44] C. Qiu, H. Chen, Q. Liu, S. Yue, H. Wang, On the solidification behaviour and cracking origin of a nickel-based superalloy during selective laser melting, Mater. Charact. 148 (2019) 330–344, https://doi.org/10.1016/j.matchar.2018.12.032.

[45] J. Xu, Y. Ding, Y. Gao, B. Liu, S. Xue, Y. Hu, D. Zhang, X. Song, Improving high-temperature mechanical properties of laser powder bed-fused Inconel 738 alloy by hot isostatic pressing: tailoring precipitates and healing defects, Mater. Sci. Eng. A 862 (2023) 144285, https://doi.org/10.1016/j.msea.2022.144285.

[46] A.S. Shaikh, M. Rashidi, K. Minet-Lallemand, E. Hryha, On as-built microstructure and necessity of solution treatment in additively manufactured Inconel 939, Powder Met. (2022) 1–9, https://doi.org/10.1080/00325899.2022.2041787.

[47] L. Chechik, K.A. Christofidou, L. Farquhar, M. Tse, G. Baxter, I. Todd, Tools for the assessment of the laser printability of nickel superalloys, Met. Mater. Trans. A 54 (2023) 2421–2437, https://doi.org/10.1007/s11661-023-07029-5.

[48] E.B. Raeker, K.M. Pusch, S.A.J. Forsik, N. Zhou, A.D. Dicus, Q.-Q. Ren, J. D. Poplawsky, M.M. Kirka, T.M. Pollock, Minor elements and solidification cracking during laser powder-bed fusion of a high gamma prime CoNi-base superalloy, Met. Mater. Trans. A 54 (2023) 1744–1757, https://doi.org/10.1007/s11661-023-06957-6.

[49] B. Mehta, K. Frisk, L. Nyborg, Advancing novel Al-Mn-Cr-Zr based family of alloys tailored for powder bed fusion-laser beam process, J. Alloys. Compd. 967 (2023) 171685, https://doi.org/10.1016/j.jallcom.2023.171685.

[50] O. Messé, R. Muñoz-Moreno, T. Illston, S. Baker, H.J. Stone, Metastable carbides and their impact on recrystallisation in IN738LC processed by selective laser melting, Addit. Manuf. 22 (2018) 394–404.

[51] O.A. Ojo, M.C. Chaturvedi, Liquation microfissuring in the weld heat-affected zone of an overaged precipitation-hardened nickel-base superalloy, Met. Mater. Trans. A 38 (2007) 356–369, https://doi.org/10.1007/s11661-006-9025-1.

[52] B.I. Kang, C.H. Han, Y.K. Shin, J.I. Youn, Y.J. Kim, Effects of boron and zirconium on grain boundary morphology and creep resistance in nickel-based superalloy, J. Mater. Eng. Perform. 28 (2019) 7025–7035, https://doi.org/10.1007/s11665-019-04419-y.

[53] M.A. Burke, J. Greggi, G.A. Whitlow, The effect of boron and carbon on the microstructural chemistries of two wrought nickel base superalloys, Scr. Metall. 18 (1984) 91–94, https://doi.org/10.1016/0036-9748(84)90096-6.

[54] K.M. Delargy, G.D. Smith, Phase composition and phase stability of a HIgh-chromium nickel-based superalloy IN939, Met. Trans. A 14A (1983) 1771–1783.

[55] B. Hu, H. Li, Neutron activated microradiography determination of boron distribution in a cast nickel-base superalloy: superalloys 1980 (1980).

[56] F. Theska, W.F. Tse, B. Schulz, R. Buerstmayr, S.R. Street, M. Lison-Pick, S. Primig, Review of microstructure–Mechanical property relationships in cast and wrought Ni-based superalloys with boron, carbon, and zirconium microalloying additions, Adv. Eng. Mater. 25 (2023) 2201514, https://doi.org/10.1002/adem.202201514.

[57] O.A. Ojo, N.L. Richards, M.C. Chaturvedi, Study of the fusion zone and heat-affected zone microstructures in tungsten inert gas-welded INCONEL 738LC superalloy, Met. Mater. Trans. A 37A (2006) 421–433.

[58] H.R. Zhang, O.A. Ojo, Cr-rich nanosize precipitates in a standard heat-treated Inconel 738 superalloy, Phil. Mag. 90 (2010) 765–782, https://doi.org/10.1080/14786430903270643.

[59] A. Després, S. Antonov, C. Mayer, M. Veron, E.F. Rauch, C. Tassin, J.-J. Blandin, P. Kontis, G. Martin, Revealing the true partitioning character of zirconium in additively manufactured polycrystalline superalloys, Addit. Manuf. Lett. 1 (2021) 100011, https://doi.org/10.1016/j.addlet.2021.100011.

[60] D. Blavette, P. Duval, L. Letellier, M. Guttmann, Atomic-scale APFIM and TEM investigation of grain boundary microchemistry in Astroloy nickel base superalloys, Acta Mater. 44 (1996) 4995–5005, https://doi.org/10.1016/S1359-6454(96)00087-0.

[61] Y. Hu, X. Yang, W. Kang, Y. Ding, J. Xu, H. Zhang, Effect of Zr content on crack formation and mechanical properties of IN738LC processed by selective laser melting, Trans. Nonferrous Met. Soc. China 31 (2021) 1350–1362, https://doi.org/10.1016/S1003-6326(21)65582-6.

[62] M. Mostafaei, S.M. Abbasi, Influence of Zr content on the incipient melting behavior and stress-rupture life of CM247 LC nickel base superalloy, J. Alloys. Compd. 648 (2015) 1031–1037, https://doi.org/10.1016/j.jallcom.2015.07.104.

[63] J.H. Schneibel, C.L. White, M.H. Yoo, On the improvement of creep strength and ductility of Ni-20 pct Cr by small zirconium additions, Met. Trans. A 16 (1985) 651–660, https://doi.org/10.1007/BF02814239.

[64] M. Thuvander, K. Stiller, Microstructure of a boron containing high purity nickel-based alloy 690, Mater. Sci. Eng. A 281 (2000) 96–103, https://doi.org/10.1016/S0921-5093(99)00741-8.

[65] Y.L. Chiu, A.H.W. Ngan, Effects of boron doping on the grain-growth kinetics and mechanical properties of γ/γ' nickel-aluminum alloys, Met. Mater. Trans. A 31 (2000) 3179–3186, https://doi.org/10.1007/s11661-000-0097-z.

[66] C.S. Pande, M.A. Imam, Grain growth and twin formation in boron-doped nickel polycrystals, Mater. Sci. Eng. A 512 (2009) 82–86, https://doi.org/10.1016/j.msea.2009.01.030.

[67] S. Antonov, A. Després, C. Mayer, G. Martin, P. Kontis, Boron trapping at dislocations in an additively manufactured polycrystalline superalloy, Materialia 30 (2023) 101801, https://doi.org/10.1016/j.mtla.2023.101801.

[68] R.P. Messmer, C.L. Briant, The role of chemical bonding in grain boundary embrittlement, Acta Metall. 30 (1982) 457–467, https://doi.org/10.1016/0001-6160(82)90226-7.
[69] R.T. Holt, W. Wallace, Impurities and trace elements in nickel-base superalloys, Int. Met. Rev. 21 (1976) 1–24, https://doi.org/10.1179/imtr.1976.21.1.1.
[70] R.F. Decker, J.W. Freeman, The mechanism of beneficial effects of B and Zr on creep-rupture properties of a complex heat-resistant alloy: the national advisory committee for aeronautics project 1478-11, Ann. Arbor., 1957.
[71] P.J. Zhou, J.J. Yu, X.F. Sun, H.R. Guan, Z.Q. Hu, The role of boron on a conventional nickel-based superalloy, Mater. Sci. Eng. A 491 (2008) 159–163, https://doi.org/10.1016/j.msea.2008.02.019.
[72] Y.L. Tsai, S.F. Wang, H.Y. Bor, Y.F. Hsu, Effects of Zr addition on the microstructure and mechanical behavior of a fine-grained nickel-based superalloy at elevated temperatures, Mater. Sci. Eng. A 607 (2014) 294–301, https://doi.org/10.1016/j.msea.2014.03.136.
[73] Z. Asqary, S.M. Abbasi, M. Seifollahi, M. Morakabati, The effect of boron and zirconium on the microstructure and tensile properties of Nimonic 105 superalloy, Mater. Res. Express. 6 (2019) 116540, https://doi.org/10.1088/2053-1591/ab4676.
[74] P. Kontis, H.M. Yusof, S. Pedrazzini, M. Danaie, K.L. Moore, P. Bagot, M.P. Moody, C. Grovenor, R.C. Reed, On the effect of boron on grain boundary character in a new polycrystalline superalloy, Acta Mater. 103 (2016) 688–699, https://doi.org/10.1016/j.actamat.2015.10.006.
[75] T.J. Garosshen, T.D. Tillman, G.P. McCarthy, Effects of B, C, and Zr on the structure and properties of a P/M nickel base superalloy, Met. Trans. A 18 (1987) 69–77, https://doi.org/10.1007/BF02646223.
[76] P. Kontis, E. Alabort, D. Barba, D.M. Collins, A.J. Wilkinson, R.C. Reed, On the role of boron on improving ductility in a new polycrystalline superalloy, Acta Mater. 124 (2017) 489–500, https://doi.org/10.1016/j.actamat.2016.11.009.
[77] K. Dörries, C. Haberland, J. Burow, J. Rösler, B. Gehrmann, C. Somsen, S. Piegert, H. Brodin, Beyond hot cracking: impact of Minor elements on a novel Ni-based superalloy for additive manufacturing, in: J. Cormier, I. Edmonds, S. Forsik, P. Kontis, C. O'Connell, T. Smith, A. Suzuki, S. Tin, J. Zhang (Eds.), Superalloys 2024, Springer Nature Switzerland, Cham, 2024, pp. 871–882.
[78] A. Després, S. Antonov, C. Mayer, C. Tassin, M. Veron, J.-J. Blandin, P. Kontis, G. Martin, On the role of boron, carbon and zirconium on hot cracking and creep resistance of an additively manufactured polycrystalline superalloy, Materialia 19 (2021) 101193, https://doi.org/10.1016/j.mtla.2021.101193.
[79] COST 50: European concerted action. https://odin.jrc.ec.europa.eu/odin/index.jsp .
[80] K. Kianinejad, R. Darvishi Kamachali, A. Khedkar, A.M. Manzoni, L.A. Jácome, S. Schriever, R. Saliwan Neumann, S. Megahed, C. Heinze, S. Kamrani, B. Fedelich, Creep anisotropy of additively manufactured Inconel-738LC: combined experiments and microstructure-based modeling, Mater. Sci. Eng. A 907 (2024) 146690, https://doi.org/10.1016/j.msea.2024.146690.
[81] A.S. Shaikh, E. Eriksson, M.H. Colliander, K. Minet-Lallemand, E. Hryha, Tailored heat treatments to enhance performance in additive manufactured HAYNES® 282® superalloy, Materialia 39 (2025) 102334, https://doi.org/10.1016/j.mtla.2025.102334.
[82] E.S. Huron, K.R. Bain, D.P. Mourer, J.J. Schirra, P.L. Reynolds, E.E. Montero, The influence of grain boundary elements on properties and microstructures of P/M nickel base superalloys. Superalloys 2004 (Tenth International Symposium), TMS, 2004, pp. 73–81, 9/19/2004 - 9/23/.
[83] S.C. Altıparmak, M. Lombardi, F. Bondioli, P. Fino, S. Biamino, D. Ugues, Hot isostatic pressing for powder-based additive manufacturing of metals: State-of-the-art review and future perspectives, J. Mater. Res. Technol. 39 (2025) 4794–4822, https://doi.org/10.1016/j.jmrt.2025.10.135.
[84] M. Kusano, Y. Takata, A. Yumoto, M. Watanabe, Effects of time per layer and part geometry on thermal history and microcracking in the fabrication of nickel superalloy samples by laser powder bed fusion, Addit. Manuf. 80 (2024) 103987, https://doi.org/10.1016/j.addma.2024.103987.
[85] Y.S. Lee, M.M. Kirka, J. Ferguson, V.C. Paquit, Correlations of cracking with scan strategy and build geometry in electron beam powder bed additive manufacturing, Addit. Manuf. 32 (2020) 101031, https://doi.org/10.1016/j.addma.2019.101031.
[86] A. Chakraborty, W. Muhammad, J.-P. Masse, R. Tangestani, M. Ghasri-Khouzani, A. Wessman, É. Martin, Role of alloy composition on micro-cracking mechanisms in additively manufactured Ni-based superalloys, Acta Mater. 255 (2023) 119089, https://doi.org/10.1016/j.actamat.2023.119089.